REPORT DOCUMENTATION PAGE

Form Approved
OMB No. 0704-0188

a. REPORT SECURITY CLASSIFICATION	1b. RESTRICTIVE MARKINGS
Unclassified	

a. SECURITY CLASSIFICATION AUTHORITY	3. DISTRIBUTION/AVAILABILITY OF REPORT
b. DECLASSIFICATION/DOWNGRADING SCHEDULE	Unlimited/Approved for Public Release

. PERFORMING ORGANIZATION REPORT NUMBER(S)	5. MONITORING ORGA AFOSR-TR-96
UILU-ENG 96-4002	0248

a. NAME OF PERFORMING ORGANIZATION	6b. OFFICE SYMBOL (If applicable)	7a. NAME OF MONIT
The Board of Trustees @ UI Grant & Contract Admin.		AFOSR/NA

c. ADDRESS (City, State, and ZIP Code)	7b. ADDRESS (City, State, and ZIP Code)
109 Coble Hall 801 S. Wright St Champaign, IL 61820	110 Duncan Ave., Room B115 Bolling AFB, DC 20332-8080

a. NAME OF FUNDING/SPONSORING ORGANIZATION	8b. OFFICE SYMBOL (If applicable)	9. PROCUREMENT INSTRUMENT IDENTIFICATION NUMBER
AFOSR/NA	NA	F49620 92-J-0280

c. ADDRESS (City, State, and ZIP Code)	10. SOURCE OF FUNDING NUMBERS F49620-92-0280			
AFOSR/NA Bolling AFB DC 20332-6448	PROGRAM ELEMENT NO. 61102F	PROJECT NO. 2308	TASK NO. A5	WORK UNIT ACCESSION NO.

1. TITLE (Include Security Classification)

Experimental Calibration of Non-Equilibrium Arc-Jet Flow Models

2. PERSONAL AUTHOR(S)
   Herman Krier, Rodney L. Burton, S.A. Bufton, T.W. Megli

3a. TYPE OF REPORT	13b. TIME COVERED	14. DATE OF REPORT (Year, Month, Day)	15. PAGE COUNT
Final Technical	FROM 6/1/92 TO 12/31/95	February 29, 1996	49 pages

5. SUPPLEMENTARY NOTATION This Final Report condenses the two Ph.D. theses of Drs. S.A. Bufton and T.W. Megli, whose research was supported by this AASERT Program

| 7. COSATI CODES			18. SUBJECT TERMS (Continue on reverse if necessary and identify by block number)
FIELD	GROUP	SUB-GROUP	

9. ABSTRACT (Continue on reverse if necessary and identify by block number)

Experimental investigations and theoretical modeling of the energy deposition and acceleration processes in 1kW-class arcjet thrusters using hydrazine propellant are presented. The report highlights detailed research in arcjet fundamentals that was reported in the two Ph.D. theses of S.A. Bufton and T.W. Megli.

We report for the first time the evidence of thermal non-equilibrium (different electron and gas temperatures). Chemical kinetics for hydrazine dissociation and ionization play important roles in the overall energy conversion. Electrostatic probe measurements at the exit plane validate the model.

19960523 205

). DISTRIBUTION/AVAILABILITY OF ABSTRACT	21. ABSTRACT SECURITY CLASSIFICATION
[X] UNCLASSIFIED/UNLIMITED ☐ SAME AS RPT. ☐ DTIC USERS	Unclassified

a. NAME OF RESPONSIBLE INDIVIDUAL	22b. TELEPHONE (Include Area Code)	22c. OFFICE SYMBOL
Dr. Mitat Birkan	(202) 767-4938	AFOSR/NA

) Form 1473, JUN 86   Previous editions are obsolete.   SECURITY CLASSIFICATION OF THIS PAGE

UNCLASSIFIED

DTIC QUALITY INSPECTED 1

**Department of Mechanical and
Industrial Engineering
University of Illinois at
Urbana-Champaign
Urbana, IL 61801**
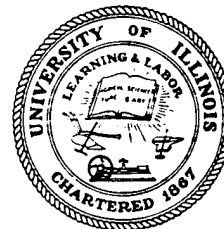
UILU-ENG 96-4002

Final Technical Report

ARCJET Fundamentals:
Experiments and Non-Equilibrium Flow Modeling

Herman Krier, Rodney L. Burton,
S. A. Bufton and T. W. Megli

Report Organization

Abstract

Experimental investigations and theoretical modeling of the energy deposition and acceleration processes in 1kW-class arcjet thrusters using hydrazine propellant are presented. The report highlights detailed research in arcjet fundamentals that was reported in the two Ph.D. theses of S. A. Bufton and T. W. Megli.[1,2]

We report for the first time the evidence of thermal non-equilibrium (different electron and gas temperatures). Chemical kinetics for hydrazine dissociation and ionization play important roles in the overall energy conversion. Electrostatic probe measurements at the exit plane validate the model.

[1]S. A. Bufton, "Exit Plane Plasma Measurements of a Low-Power Hydrazine Arcjet," Ph.D. Thesis, Department of Mechanical and Industrial Engineering, University of Illinois, 1995.

[2]T. W. Megli, "A Nonequilibrium Plasmadynamics Model for Nitrogen/Hydrogen Arcjets," Ph.D. Thesis, Department of Mechanical and Industrial Engineering, University of Illinois, 1995.

MEASURED PLASMA PROPERTIES AT THE
EXIT PLANE OF A 1 kW ARCJET

Abstract

With recent advances made in low power (1-2 kW) arcjet numerical modeling, validation of numerical models through experimentation has become increasingly important. We describe multiple electrostatic probe techniques for characterizing flow conditions at the exit plane of a 1 kW-class hydrazine thruster. An improved electrostatic quadruple probe technique, which is also modified to account for plasma gradients over the finite probe volume and multiple ion species, provides measurements of n_e, T_e and u_i/c_m at the thruster exit. Quadruple probe results are also presented for measurements at several centerline locations immediately downstream of the thruster exit plane. A spatially-resolved time-of-flight electrostatic probe technique is employed for measurements of radial profiles of the plasma axial velocity u_i. The quadruple probe results (T_e, n_e, u_i/c_m), coupled with independent measurements of plasma velocity, are used to estimate ion temperature $T_i = T_g$ and the extent of thermal non-equilibrium at the thruster exit. Exit plane experimental data for u_i, T_e and T_g are compared with computational arcjet model predictions, showing agreement for u_i and T_g. The model underpredicts T_e and a direct comparison of n_e results is precluded by large axial gradients at the thruster exit.

Nomenclature

A	Electrode geometric surface area [m^2]
c_m	Most probable thermal speed [m/s]
e	Electron charge [coulombs]
f	Ion composition parameter ($=n_{H^+}/n_e$)
I	Probe electrode current [A]
I_{arc}	Arcjet operating current [A]
j_i	Ion saturation current density [A/m^2]
k	Boltzmann constant [J/K]
m	Particle mass [kg]
$\dot{m}$	Propellant flow rate [mg/s]
n	Particle density [cm^{-3}]
P	Thruster power [kW]
P_k	Designation for electrode "k"
Q	Collision cross section [m^2]
r_p	Electrode radius [mm]
s	Electrode clearance [mm]
T	Temperature [K, eV]
u_i	Ion flow velocity [m/s]
v	Particle thermal speed [m/s]
V	Probe electrode voltage [Volts]
V_d	Electrode relative bias voltage [Volts]
V_f	Floating electrode voltage [Volts]
V_p	Plasma potential [Volts]
V_{arc}	Arcjet operating voltage [Volts]
x	Axial distance from thruster exit [mm]
x_{H^+, N^+}	Wake effect collection area parameters
δ	Flow divergence angle [Degrees]
ε_d	Dissociation energy [eV]
Γ	Mathematical Gamma function

θ	Probe angle [Degrees]
κ	Correction to n_e from N^+ ions
μ	Equal to $(m_{H^+}/m_{N^+})^{1/2}$
τ_L	Electrode "end effect" parameter
λ_D	Debye length [m]
λ_{mfp}	Collision mean free path [m]
σ	Standard deviation [mm]
ϕ	Equal to e/kT_e, [V^{-1}]

Subscripts

e,i,n	Electron, ion, neutral species
g	Gas
$1,2,3,4$	Electrode designation

I. Introduction and Background

Although research in the area of electrothermal thrusters is relatively mature, only recently has the arcjet become applied to commercial satellites.[1] With these thrusters beginning to find a niche in industry, accurate numerical models become increasingly important as design tools to help in the understanding of fundamental arcjet physics. As such, adequate measurements of fundamental plasma properties must be available for the purpose of validating numerical efforts. It is the purpose of this research to: 1) provide fundamental data for validation of H_2/N_2 computational arcjet models; 2) add to the existing base of fundamental data in the very near-field plume region; and 3) demonstrate the feasibility of electrostatic probing techniques as useful diagnostics in the small geometries associated with the 1 kW arcjet. In this paper we present electrostatic time-of-flight and quadruple probes results for the exit plane of a 1 kW hydrazine arcjet. Where applicable, comparisons are made with experimental data and computational model predictions performed by our group.

Electrostatic probes have found much use in experimentally determining plasma parameters in space and laboratory plasmas. Several authors[2-6] have employed classical Langmuir[7] single probes in the characterization of low power arcjet plumes. While single probes are appealing due to their relatively simple construction, interpreting the probe V-I characteristic can be difficult. A viable alternative is the triple electrostatic probe,[8] which allows simultaneous measurement of T_e and n_e without the necessity of a voltage sweep and a corresponding probe V-I characteristic. The utility of triple probes for electric propulsion devices has been demonstrated in MPD thruster plumes[9-12] and in a 1 kW hydrogen arcjet plume.[13] Additionally, a general review[14] of electrostatic probe techniques and their uses in electric propulsion devices has recently been presented.

Under certain conditions, the crossed-probe technique[15-18] can be used to measure u_i/c_m (=plasma velocity/ion most probable thermal speed) in flowing plasmas. The quadruple electrostatic probe[19] combines the crossed-probe and triple probe techniques for simultaneous measurements T_e, n_e, and u_i/c_m. The utility of the quadruple probe has been demonstrated in an MPD thruster[19,20] and, more recently, in the very near-field plume of a 1 kW hydrazine arcjet.[21]

II. Quadruple Probe Technique

Figures 1a. and 1b. show an electrical schematic and potential plot of the quadruple probe, consisting of three cylindrical electrodes (P$_1$, P$_2$, P$_3$) which are aligned with the plasma flow vector and one electrode (P$_4$) which is perpendicular to the plasma flow. P$_3$ and P$_4$ are biased at constant voltages V_{d3} and V_{d4} relative to P$_1$, and P$_2$ assumes the floating potential V_f of the local plasma ($I_2=0$). The circuit comprised of electrodes 1, 3

and 4 is electrically floating such that ion current collected at P_3 and P_4 is balanced by the electron current collected at P_1, thereby determining the potential difference V_{d2} [$=V_{d2}(T_e)$]. The three aligned electrodes 1-3 are similar to the triple probe and yield simultaneous measurements of n_e and T_e. The addition of the perpendicular electrode P_4 allows the measurement of the parameter u_i/c_m, determined from the ratio I_4/I_3 for crossed electrostatic electrodes with $V_{d3} = V_{d4}$. For the quadruple probe, the measured quantities are the electrode currents I_3 and I_4 and the potential difference between electrodes 1 and 2, V_{d2}. Currents I_3 and I_4 are determined by measuring voltage drops across resistors ($R_3 = R_4 = 100 \Omega$). The electrode bias voltages V_{d3} and V_{d4} are provided by batteries, with $V_{d3}=V_{d4}=12V$.

It has been shown[9] that probe contamination can have a marked effect on T_e measurements through drastic changes in the measured quantity V_{d2}. In the present study, the probe was cleaned thoroughly before each data acquisition session using ion bombardment cleaning.[13] This was accomplished by biasing all four electrodes 24 V below facility ground to attract ions to the probe. The electrodes were then placed in the arcjet plasma stream for several ~ 1 s intervals, so that the electrodes would glow and "burn off" the contaminant layer. Quadruple probe sweeps acquired before cleaning always yielded electron temperatures that were higher than the post-cleaning values by a factor of ~ 2.

Probe Construction

A schematic of the quadruple probe used in this study is shown in Fig. 2. The probe is comprised of 4 individual tungsten wire electrodes of 0.25 mm diameter with an exposed length of 2.5 mm for electrodes 1-3 and 2.0 mm for electrode 4. The location of the perpendicular electrode has been modified from that of previous probes,[21] to coincide with the axial location of the probe center. Each wire is mounted in round single-bore alumina (Al_2O_3) tubing, which is in turn mounted in, and supported by, thin-wall stainless steel tubing. This assembly is mounted in a larger stainless steel tube to facilitate connecting the probe tip to the probe positioning mechanism discussed below. Inside this larger tubing is a four-bore alumina tube that electrically insulates the four probe leads. A high temperature ceramic-based adhesive[22] is used to bond each of the probe electrodes and components in place. A small quantity of adhesive is placed at the junction between P_4 and its single bore alumina tube to electrically insulate part of the electrode, thereby reducing the error associated with determining its geometric surface area (Fig. 2.).

The center-to-center separation between electrodes 1 and 2 is 1.4 mm. This spacing, along with electrode lengths of 2.5 mm, allows an unaligned quadruple probe to handle flow divergence angles $\delta \sim 30°$ without "shadowing" of one electrode by the other. In an effort to minimize the effect of the probe geometry on the plasma flow, a gradual transition between the electrodes and the probe support has been implemented. The radius of the single-bore alumina electrode supports is ~ 0.4 mm, which minimizes perturbations of the plasma flow at the junction between the electrodes and their support. The exposed length of the single-bore alumina is ~ 5 mm. Ceramic adhesive is used to fill the void, and ease the transition, between the electrodes and the stainless steel probe support tubing.

Probe Length Scales

For the conditions expected at the exit plane probe location ($T_e \sim 0.6$ eV, $n_e \sim 4 \times 10^{12}$ cm^{-3}), the Debye length is 2.9×10^{-4} cm and the ratio of electrode radius to Debye length $r_p/\lambda_D=45$, so that the ion sheath surrounding the electrodes can be classified as thin with

minimal error. For probe measurements 5 mm downstream, this ratio increases to r_p/λ_D ~ 55. The clearance (s) between electrodes 1 and 3 (Fig. 2) is s~1 mm so that $s/\lambda_D > 250$ and the sheaths on adjacent electrodes do not interact.

To avoid strong sensitivity of the ion current to small misalignments between the flow vector and the electrode axis, the so-called end effect parameter[23] τ_L $[=(L/u_i\lambda_D)(kT_e/m_i)^{1/2})]$ should be greater than 50. For our plasma conditions, this parameter is conservatively estimated at $\tau_L > 250$. The electrodes should also be long enough that the Bohm sheath ion current collected along the cylinder length (I_b) is much larger than the current collected at the probe end due to the convection of charged particles into the probe tip (I_t). A first order analysis of the ratio I_b/I_t for the conditions at the exit plane showed $I_b/I_t > 30$, so that the error introduced to the collected ion current by neglecting the cylinder tip is less than 4%.

The radius r_p of the tungsten electrodes (Fig. 2) was chosen as a compromise between the thin sheath assumption ($r_p/\lambda_D >> 1$) and the assumption of free molecular flow over the probe electrodes ($\lambda_{mfp}/r_p >> 1$). For the seven species plasma expected at the exit plane (H_2, N_2, H, N, H^+, N^+, e), all relevant collision mean free paths were calculated. The following assumptions are made in calculating mean free paths: T_e=7000 K, T_g=2500 K, $n_e = 4 \times 10^{12}$ cm^{-3}, and $n_{neutral} = 3 \times 10^{15}$ cm^{-3} with 10% dissociation at the thruster exit. The following (worst case) mean free paths were calculated: $\lambda_{n-n}/r_p > 20$, $\lambda_{i-n}/r_p > 5$, $\lambda_{i-i}/r_p > 30$, $\lambda_{i-e}/r_p = 20$, $\lambda_{e-n}/r_p > 20$, and $\lambda_{e-e}/r_p = 30$. Clearly, the probe electrodes are operating in the collisionless regime. Additionally, $\lambda_{mfp}/\lambda_D > 200$ for all collisions, with an overwhelming majority of the collisions having $\lambda_{mfp}/\lambda_D > 1000$, indicating that the collisionless sheath assumption is appropriate.

Quadruple Probe Theory

Quadruple probe analysis assumes: 1) The ion sheath surrounding the tungsten wires is thin compared to the wire radius ($r_p >> \lambda_D$); 2) Each probe wire and sheath are collisionless ($\lambda_{mfp} >> r_p >> \lambda_D$); 3) The electron energy distribution is Maxwellian; 4) Velocity slip between plasma species is negligible; and 5) A wake region of low ion and electron density exists downstream of the perpendicular electrode P_4.

Derivation of quadruple probe response is similar to that of the triple probe[8] and has been presented elsewhere.[19-21] In our previous work[21] we presented some of the revisions necessary to allow the application of triple and quadruple probe theory to multicomponent (N-H) plasmas. In the present study, the probe is applied to a simulated hydrazine plume, with multiple species of ions present, whereas most of the previous applications of triple and quadruple probes have been for plasmas with one dominant species of positive ion. Single Langmuir probes have been used in nitrogen and hydrogen-based arcjet plumes,[2-5] but their use is not contingent on knowledge of the species.

In the present study, we present a significant modification of the quadruple probe theory. Rather than utilizing an analytic expression for the current collected at electrode P_4, I_4 is related to the current collected at P_3 through the ratio of the measured quantities I_3 and I_4. The significance of this modification is that it completely removes errors in T_e and n_e measurements that were due to assumptions regarding effective current collection area of P_4. For a quadruple probe with electrode geometric surface areas A_3 (=A_1=A_2) and A_4 and electrode biasing such that $V_{d3}=V_{d4}$, the following expres-sion can be derived:

$$1 = \frac{1 + \exp(\phi V_{d3}) - 2\exp[\phi(V_{d3}-V_{d2})]}{(I_4/I_3)\{\exp[\phi(V_{d3}-V_{d2})]-1\}} \tag{1}$$

Since V_{d3} is prescribed and V_{d2} is experimentally determined, Eq. (1) determines $T_e = e/k\phi$ through iteration.

The ion saturation current density j_i is related to measured quantities by

$$j_i = \frac{(I_3/A_3)(1 + I_4/I_3)}{\exp(\phi V_{d2}) - 1} \tag{2}$$

Eq. (2) is used to determine n_e from I_3, I_4 and V_{d2} by relating j_i to the electron density through the Bohm sheath analysis. For a plasma with more than one species of collected ion, the Bohm analysis must be modified to account for the collection of each ion species via the Bohm sheath. For the region of the hydrazine plume of interest, H^+ and N^+ are the dominant ions species, and the Bohm expression becomes:[21]

$$j_i = e(kT_e)^{1/2}\exp\left(-\frac{1}{2}\right)\left(\frac{n_{H^+}}{(m_{H^+})^{1/2}} + \frac{n_{N^+}}{(m_{N^+})^{1/2}}\right) \tag{3}$$

For $n_e = n_{H^+} + n_{N^+}$, Eqs.(2) and (3) yield

$$n_e = \frac{\kappa\left(\frac{I_3}{A_3}\right)\left(1 + \frac{I_4}{I_3}\right)\exp\left(\frac{1}{2}\right)(m_{H^+})^{1/2}}{e(kT_e)^{1/2}\left[\exp(\phi V_{d2}) - 1\right]} \tag{4}$$

In Eq. (4), κ represents the effect of multiple ion species on the probe response to electron density:

$$\kappa = \frac{1 + \left(\frac{n_{N^+}}{n_{H^+}}\right)}{1 + \mu\left(\frac{n_{N^+}}{n_{H^+}}\right)} \tag{5}$$

where $\mu = (m_{H^+}/m_{N^+})^{1/2}$. For a plume contain-ing only H^+, $n_{N^+} = 0.0$ and κ reduces to unity, such that Eq. (4) reduces to single component (H^+) form.

Experimental observations[24,25] show that low nitrogen ion densities are found near the exit plane in ammonia and hydrazine arcjets. It is suggested that this is a result of charge exchange collisions in the expanding nitrogen-hydrogen propellant. It can be shown (Fig. 3) that equilibrium number density ratios n_N/n_H and n_N^+/n_H^+ are equal for $T < 7500$ K at $p = 1$ atm. For this temperature range, $n_N/n_H < 0.4$, due to the preferential dissociation of H_2 ($\varepsilon_d = 4.48$ eV) over N_2 ($\varepsilon_d = 9.61$ eV). The arcjet exit plane N-H plasma is highly dissociated and partially ionized, with $T_e > T_g$, and the estimated range of gas temperature is $T_g < 6000$ K. Ionization by electron collision is negligible, and nitrogen rapidly undergoes charge-exchange collisions with hydrogen, the cross-section for which is on the same order of magnitude as N-H momentum transfer collisions. Thus: $H + N^+ \longleftrightarrow H^+ + N$, and in the absence of other ionization processes, the two charge-exchange reactions balance in steady state. Writing these volumetric collision rates in the form nQv, with relative thermal speeds $v_{H,N} \approx v_H$, and cross sections $Q_{H-N^+} \approx Q_{N-H^+}$ gives:

$$\frac{n_{N^+}}{n_{H^+}} = \frac{n_N}{n_H} \tag{6}$$

which directly implies a low nitrogen ion density in the exit plane (Fig. 3). Thus, the nitrogen ion density is effectively determined by the gas temperature T_g and not the electron temperature. For $T_g < 6000$ K, $n_N^+/n_H^+ < 0.1$ and $\kappa < 1.07$, indicating a ~7% increase of n_e due to the presence of nitrogen ion probe current.

Crossed Electrostatic Probes

The use of crossed electrostatic probes for measuring plasma velocity[15,17] and the implementation of the crossed probe technique into the quadruple probe have been presented elsewhere.[19,21] For a cylindrical electrode oriented at an angle θ relative to the plasma flow, the collected ion current is a function of the quantity $(u_i/c_m)\sin\theta$, where $c_m = (2kT_i/m_i)^{1/2}$. For the case of two equally biased probes, with one probe aligned with the flow vector and the other one normal to it, the single species collected ion current ratio for the thin sheaths case is:[17]

$$\frac{I_4}{I_3} = \frac{2\,A_4}{\sqrt{\pi}A_3} \exp\left[-\left(\frac{u_i}{c_m}\right)^2\right] \sum_{n=0}^{\infty} \left[\frac{\left(\frac{u_i}{c_m}\right)^n}{n!}\right]^2 \Gamma(n+\tfrac{3}{2}) \tag{7}$$

In order to apply the crossed probe technique to the multicomponent (H_2-N_2) plasmas of interest here, significant revisions must be made to Eq. (7). In the original derivation of the crossed probe technique, a Maxwellian velocity distribution is assumed for the single component ion collection.[15] For the present study, this expression has been rederived using a two-component form of the Maxwellian velocity distribution. The derivation is similar to the single component case, and results in a contribution to the ratio I_4/I_3 from each of the collected ion species. For the two species of ions assumed present, the ion composition is defined by $f = n_{H^+}/n_e$ and $(1-f) = n_{N^+}/n_e$ ($n_e = n_{H^+} + n_{N^+}$). The resulting expression for the measured current ratio is

$$\frac{I_4}{I_3} = C\left\{ f(x_{H^+})\exp\left[-\left(\frac{u_i}{c_{m,H^+}}\right)^2\right] \sum_{n=0}^{\infty} \left[\frac{\left(\frac{u_i}{c_{m,H^+}}\right)^n}{n!}\right]^2 \Gamma(n+\tfrac{3}{2}) \right.$$
$$\left. +\mu(x_{N^+})(1-f)\exp\left[-\left(\frac{u_i}{\mu c_{m,H^+}}\right)^2\right] \sum_{n=0}^{\infty} \left[\frac{\left(\frac{u_i}{\mu c_{m,H^+}}\right)^n}{n!}\right]^2 \Gamma(n+\tfrac{3}{2}) \right\} \tag{8}$$

where the constant C is given by

$$C = \frac{2\,A_4}{\sqrt{\pi}\,A_3\left[f + (1-f)\mu\right]} \tag{9}$$

In Eq. (8), the first term in the brackets { } is the H^+ contribution and the second term is the N^+ contribution. The most probable thermal speed for N^+ (c_{m,N^+}) has been written in terms of c_{m,H^+} (since $c_{m,N^+} = \mu\, c_{m,H^+}$). Note that each of the terms is weighted by the relative density of its corresponding ion [f, $(1-f)$].

Because a wake is formed behind P_4, a portion of the electrode area A_4 does not collect ions. The parameters x_{H^+} and x_{N^+} are the fractions of the electrode area A_4 available for H^+ and N^+ collection, respectively. Because the extent of the wake effect is determined by the relative magnitudes of the directed ion velocity u_i and thermal speed

of the ions, x_{H+} and x_{N+} are not necessarily equal. For $T_g=T_i=2500$ K and a directed velocity $u_i \sim 6500$ m/s, $u_i/c_{m,H+} \sim 1$ and $u_i/c_{m,N+} \sim 4$. Several references discuss the wake effect for high speed flows.[17-19] It has been postulated and experimentally verified for an argon plasma at $u_i/c_m \sim 1$, that the wake effect causes the effective collection area to be half of the geometric electrode area.[17] Since $u_i/c_{m,H+}$ is expected to be ~ 1, x_{H+} is assumed to be $1/2$ so that only the front half of P_4 collects ions. For the nitrogen ions, the wake effect reduction in collection area is expected to be more pronounced. Since the directed velocity u_i is several times $c_{m,N+}$, N^+ is assumed to be collected by the projected area[19] of the perpendicular electrode only, such that $x_{N+}=1/\pi$.

Given f, Eq. (8) becomes an expression for $u_i/c_{m,H+}$ versus the measured current ratio I_4/I_3. Equation (8) is plotted in Fig. 4 for $0 \leq f \leq 1$, $x_{H+}=1/2$ and $x_{N+}=1/\pi$. Pure H^+ collection is represented by f=1.0, $2H^+ + N^+$ collection by f=0.67, and pure N^+ collection by f=0.0.

If an independent measure of the directed plasma velocity u_i is known, Fig. 4 can be used to determine $c_{m,H+}$ $[=(2kT_i/m_{H+})^{1/2}]$ and, hence, the gas temperature $T_g=T_i$. We describe below u_i measurements which lead to an estimate of T_i.

Effect of Radial Gradients on Probe Response

Quadruple probe measurements at the thruster exit plane show smooth symmetric profiles for n_e and the electrode currents I_3 and I_4, as shown below. However, V_{d2} is known to have a very asymmetric profile,[21] which is interpreted as a result of the steep radial gradient in n_e off-axis, and to a lesser extent, the radial gradient in T_e. These gradients are perpendicular to the quadruple probe electrodes and the arcjet thrust axis. In the presence of plasma radial gradients, the individual electrode current equations[20] are rewritten in terms of the plasma parameters at each electrode, and are rearranged to solve explicitly for V_{d2} and I_3 in terms of radial profiles of T_e and n_e:

$$V_2=V_2 \ (T_{e2},\kappa) \tag{10}$$
$$V_1=V_1 \ (T_{e1}, T_{e3}, n_{e1}, n_{e3}, I_4/I_3, \kappa) \tag{11}$$
$$V_{d2}=V_2 - V_1 \tag{12}$$
$$I_3=I_3 \ (T_{e3}, n_{e3}, \kappa) \tag{13}$$

The subscripts on the parameters T_e and n_e in Eqs. (10)-(13) denote the local value of those parameters at each of the electrodes (1-3) of the quadruple probe. The ratio I_4/I_3 is a measured quantity and κ is a function of the plasma composition discussed above. Since the centerline experimental data are at zero gradient conditions, these data can be used with Eqs. (1) and (4) to determine the centerline values of T_e and n_e.

Using Eqs. (10)-(13), Fig. 5 displays V_{d2} vs. radial position for the quadruple probe of Fig. 2, for flat and Gaussian n_e and T_e profiles. For Gaussian n_e and constant T_e, V_{d2} increases monotonically across the thruster. For a Gaussian T_e distribution broader than n_e, the V_{d2} profile shows more asymmetry. The constant T_e case can be solved analytically for V_{d2}, giving:

$$V_{d2} = \frac{kT_e}{e} \ln\left[\left(1+\frac{I_4}{I_3}\right)\times\left(\frac{n_{e3}}{n_{e1}}\right)+1\right] \tag{14}$$

In this equation the effect of the density gradient can be clearly seen. As the swept probe starts outside the plume and enters it, $n_{e3}/n_{e1} < 1$. At the axis $n_{e1} = n_{e3}$, and as the probe leaves the plume, $n_{e3}/n_{e1} > 1$. The result [Eq. (14)] is a monotonically increasing V_{d2} across the thruster face.

Given arbitrary profiles of $T_e(r)$ and $n_e(r)$, we see that $V_{d2}(r)$ and $I_3(r)$ can be predicted. The inverse problem, of extracting n_e and T_e profiles from measured V_{d2} and I_3, can also be solved. Since V_{d2} [Eq. (12)] is a strong function of T_e, and I_3 [Eq. (13)] is a strong function of n_e, there is sufficient uncoupling that an iterative routine is used to find the unique $T_e(r)$ and $n_e(r)$ profiles which reproduce the measured V_{d2} and I_3 profiles. Starting with centerline values and assumed Gaussian profiles, the routine marches the probe position across the thruster face, while generating a new T_e profile. This updated profile is used with Eq. (13) to update $n_e(r)$, and the process is repeated until both profiles converge. Typically five numerical iterations are required to reach convergence.

III. Time-of-Flight Velocimetry

Since in addition to the quantities n_e and T_e a quadruple probe measurement yields the quantity $u_i/(2kT_i/m_{H^+})^{1/2}$, knowledge of the heavy particle velocity u_i can be used to determine the heavy particle temperature $T_g = T_i$. We have designed and implemented a time-of-flight velocimetry technique for measuring spatially resolved axial velocities in arcjet plumes. This technique is derived from a previous Current Modulation Velocimetry (CMV) method.[13,26] In our method, a short duration current deficit is superimposed on the arcjet current, the effect of which is monitored by an electrostatic time-of-flight (T-O-F) probe as it convects axially in the thruster plume.

Time-of-Flight Probe

The CMV technique can be made spatially resolved with electrostatic probes, thereby eliminating the need to Abel-invert the data as required by line-of-sight optical methods. Figure 6 shows the electrostatic time-of-flight sensing probe used in this study. It consists of two 0.75 mm diameter tungsten wires which are electrically insulated along most of their length by two 1.6 mm o.d. alumina tubes. The exposed length of each tungsten electrode is 0.25 mm and the axial separation between the two is 5 mm ($\pm$ 2%). The elevation of the probe is such that the arcjet thrust axis is located between the sensing electrodes. The electrodes are biased 24 V below facility ground (arcjet anode) to monitor the local electron saturation current density [$\sim n_e, (T_e)^{1/2}$] at each measurement location. Variations in probe electrode saturation currents are monitored as they convect over the two T-O-F electrodes, with the temporal separation of these signals, combined with the probe geometry, indicating the flow velocity.

Although this probe is physically intrusive, the probe electrodes (0.75 mm dia.) are in the near-free molecular flow regime and are thus expected to have little effect on the flow. Additionally, any plasma perturbations due to the electrodes (shocks, collisional effects, etc.) are expected to have a similar result at each electrode, thereby having minimal effect on the convective time delay.

Arcjet Current Deficit Circuitry

The arcjet power processing unit (PPU) produces current with a high frequency ripple ($\sim$ 15-20 kHz, $\pm$ 8% about the mean) which causes "natural" fluctuations in n_e and T_e. These inherent fluctuations are difficult to utilize with the T-O-F probe due to their long period ($\sim$ 55 μs), compared with the expected convective time delay of the T-O-F probe ($\sim$ 1 μs). Instead, fluctuations are artificially introduced to the arcjet plasma flow by superimposing a short duration ($\sim$ a few μs) current deficit pulse on the arcjet operating current.

8

The circuit used to modify the arc current is similar to that used in previous CMV studies[26] and is shown in Fig. 7. The current pulse is initiated by closing a switch to a fast R-C circuit in parallel with the arcjet, causing a sudden decrease in arc current while the capacitor charges. This short duration ($\sim$ 4 μs) current deficit results in a "tagging" of the plasma in the arc-heating region. Switch closure is accomplished with an IRF-350 field-effect transistor (FET), which is closed by the gate pulse shown in Fig. 7. Originally, the R-C circuit element was replaced by a single resistor (20-30 Ω), but ringing on the edges of the resulting square current pulse obscured the desired T-O-F probe signals.

Spatially resolved axial velocities are measured by triggering the arcjet current deficit pulse at several different T-O-F probe locations. Since the probe is swept radially through the plume during the experiment, it is necessary to trigger the current deficit pulse repeatably at each desired radial location. Probe location is measured by monitoring the voltage of a precision potentiometer (Fig. 7) which has been calibrated against the arcjet anode for probe position. The position (voltage) of the desired measurement location is set at the voltage comparator circuit, so that a trigger signal is issued to the HP 214A pulse generator when the probe reaches the desired radial location. In turn, the pulse generator supplies a square pulse to "close" the FET and initiate the arcjet current deficit. Because 1) the gate pulse must be positive (relative to the FET voltage), and 2) the arcjet cathode (and FET) operates at $\sim$ -100 V (anode grounded), the FET Driver Circuit (Fig. 7) is a necessary buffer between the FET and the HP pulse generator. Since the probe is swept relatively slowly ($\sim$ 20 cm/s), the probe location is effectively "frozen" during the $\sim$ 3-4 μs elapsed time between the initial trigger and the monitoring of the tagged plasma at the T-O-F electrodes.

IV. Experimental Apparatus

Electrostatic probe experiments were carried out at the exit plane of a 1 kW NASA arcjet thruster[27] operating at a flow rate of 50 mg/s of 2H_2 + N_2 to simulate fully decomposed hydrazine. Each component of the propellant was individually metered by Unit mass flow controllers and mixed in the propellant line. During steady state operation, the thruster operated at 10.0 A and 112 V ($P/\dot{m}$ = 22.4 MJ/kg). Arc current was measured with a Hall effect current transducer. The thruster exhausted into a 1 m diameter x 1.5 m long vacuum tank[21] at $\sim$200 mTorr during arcjet operation. Anode temperatures were monitored with an optical pyrometer, reaching $\sim$ 1200 K during steady state operation.

The quadruple probe and T-O-F probe are accurately positioned and repeatably swept through the thruster plume with the probe mount system shown in Fig. 8. The complete assembly is fastened to a step motor (Fig. 8) mounted on a linear translation carriage.[21] The motor and probe assembly carriage is capable of $\pm$ 5 cm linear translation perpendicular to the arcjet axis, allowing the probes to be manually swept through the plume at $\sim$ 20 cm/s. Carriage and probe position are determined to 0.25 mm by a precision 10 kΩ linear potentiometer coupled to the carriage manual drive shaft, and calibrated against the outer diameter of the anode. The probe support arm is coupled directly to the motor shaft with the probe tip on the shaft axis, allowing probe angle to be varied (in 0.9° increments) without changing the probe tip location.

Probe elevation is repeatably located to within 0.5 mm by aligning the probe center with a line etched on the arcjet anode. The separation between the probe tips and the thruster exit plane is reliably set to within 0.1 mm with a spark gap gauge. The arcjet mount is known to deflect toward the probe $\sim$0.7 mm while under vacuum. Any error

associated with the arcjet exit plane position because of this is systematic and does not affect the relative spacing of subsequent axial measurement positions.

V. Experimental Results and Analysis

Experimental quadruple and T-O-F probe results are presented for the very near-field plume of the arcjet. To quantify the extent of axial gradients in T_e and n_e, quadruple probe measurements are made at several probe tip locations from 1-5 mm from the exit plane. Radial profiles with probe tips located 1 mm from the exit are presented for both the quadruple and T-O-F probes.

Quadruple Probe Results

For the quadruple probe, T_e and n_e are determined by measurements of V_{d2}, I_3 and I_4. Since these parameters are expected to be influenced by the inherent current ripple associated with the arcjet PPU, a discussion of the effect of the ripple on the probe is warranted. Figure 9 shows the centerline ion current density j_3 (= I_3/A_3) measured at electrode 3 and the arc current I_{arc} versus time. The current measured at electrode 3 is in phase with the arc current, except for a delay of ~ 3-4 μs associated with the time required for the plasma to flow from the arc-heating region near the cathode to the quadruple probe. Accounting for differences in average velocity and measurement location, this delay is consistent with previous triple probe results for the hydrogen arcjet.[13]

The relationship between centerline measurements of V_{d2} and j_3 is shown in Fig. 10. While j_3 closely follows the phase of the PPU current ripple, V_{d2} is 180° out of phase with j_3. Since $j_3 \sim n_e(T_e)^{1/2}$ and V_{d2} increases monotonically with T_e [Eq. (1)], Figs. 9 and 10 indicate that, except for the convective time delay, n_e increases and T_e decreases with increases in I_{arc} during a typical PPU ripple cycle. Specifically, Eqs. (1) and (4) indicate that the ± 10% current ripple causes an associated ± 18% ripple in n_e (in phase) and a ± 5% ripple in T_e (180° out of phase) about their means. For the quadruple probe centered at x=2.25 mm from the exit plane, the mean centerline values are T_e ~0.6 eV and n_e ~3.6 x 10^{12} cm^{-3}. The T_e results, although out of phase with I_{arc}, are in phase with the arc voltage V_{arc} (which has a ± 3% ripple) due to the negative impedance characteristic of the arcjet. Thus the T_e behavior is consistent with the variation of the E-field, which heats the electrons. These results are different from previous hydrogen arcjet data,[13] which indicate that n_e decreases and T_e increases with increasing I_{arc}. It is unclear at this time if this is an indication of a fundamental difference in the operating physics of the hydrazine and hydrogen arcjets.

Because of the large variation in the measured quantities V_{d2}, I_3 and I_4 with the PPU current, the mean values of these parameters are used to determine the mean values of T_e, n_e and $u_i/c_{m,H^+}$ through Eqs. (1), (4) and (8). For radial profile data, a moving average smoothing routine is applied to the raw data so that the effects of the PPU ripple are eliminated.

T_e and n_e Axial Profiles

Previous n_e data indicate that axial gradients over the length of the quadruple probe may be large.[4,28,29] To quantify the effects of gradients in T_e and n_e over the 2.5 mm quadruple probe length, centerline data were acquired for several probe axial locations. Five probe tip locations from 1 to 5 mm from the thruster exit, in 1 mm increments, were utilized. Results for the measured current density j_3 for five centerline axial locations are shown in Fig. 11. The geometry of the three aligned electrodes is also shown, with its placement corresponding to the probe location for the first axial location. A 50 %

decrease in j_3 is indicated over the 5 mm region investigated, which represents the combined effect of changes in T_e and n_e, since $j_3 \sim n_e(T_e)^{1/2}$.

Figure 11, along with the corresponding V_{d2} data and Eqs. (1) and (4), yields the axial centerline profiles of T_e and n_e shown in Fig. 12. As a check of the quadruple probe and to insure that the presence of the perpendicular electrode does not influence the T_e and n_e data, independent measurements were made with a triple probe at the first axial location (x= 2.25 mm). The quadruple and triple probe T_e and n_e data were consistent within 5 %, well within the experimental error associated with the experiment. This is not a surprising result, since in the limit $I_4/I_3 \dashrightarrow 0$, Eqs. (1) and (4) reduce to the triple probe equations for T_e and n_e.

The electron temperature (Fig. 12) varies from 6700 to 3600 K (~0.6 - 0.3 eV) between 2.25< x <6.25 mm from the thruster exit. These results are roughly consistent with previous far-field plume results of T_e ~0.2-0.3 eV for 30<x<150 mm and T_e ~ 0.1-0.2 eV for x=320 mm.[3,4] Further, the present data seem to corroborate previous estimates[28] of $T_e \geq 0.5$ eV in the arcjet nozzle based on arguments that T_e is on the order of the atomic excitation temperature.

Results for the electron density axial profile are also shown in Fig. 12. Over the 5 mm range of probe locations n_e drops by ~ 30 %, with the magnitude of dn_e/dx increasing slightly near the thruster exit. The n_e results of the present study, along with those of other researchers, are summarized in Fig. 13. While the n_e gradient based on the present data is large near the exit (dn_e/dx ~ - 0.5 x 10^{12} cm^{-3}/mm at x= 2-3 mm), it is small compared with the axial gradient indicated in the nozzle interior and at the exit plane. It thus appears likely that large axial variations in the n_e gradient (large d^2n_e/dx^2) are present in the thruster very near-field plume. The present n_e data appear consistent with previous results with the exception of previous data for x=0 and x=10 mm (Fig. 13).[29] However, these data represent upper limits placed on n_e based on Stark broadening of line-of-sight (non-Abel inverted) emission spectroscopy signals, and thus are consistent with our probe results.

Based on the axial variations of T_e and n_e reported above, it is apparent that the quadruple probe results represent plasma conditions averaged over the axial dimension (2.5 mm) of the probe. Additionally, the very large n_e gradients presumed to exist immediately downstream of the thruster exit require extra care in locating and reporting probe positions for both optical and intrusive measurement techniques.

Exit Plane Radial Profiles

Traces for the measured quadruple probe voltage V_{d2} and current I_3 are shown for a typical exit plane radial sweep in Fig. 14. These data have been smoothed so that the traces shown represent the mean signals (with the PPU ripple effects removed). As discussed above, the I_3 trace is symmetric about the thruster centerline, while the V_{d2} trace exhibits the asymmetry attributed to radial gradients in n_e and, to a lesser extent, T_e over the probe face.[21] The modified quadruple probe theory [Eqs. (10)-(13)] is used to solve for the radial profiles $T_e(r)$ and $n_e(r)$ resulting from the radial quadruple probe data V_{d2} and I_3 (Fig. 14). This analysis indicates that the T_e profile is very flat near the centerline (r<3 mm) and nearly uniform at T_e ~ 0.6 eV. This uniform T_e, along with Eq. (13), is used to determine the radial n_e profile at x=2.25 mm from the thruster exit, shown in Fig. 15. Uncertainty in n_e values far from the centerline is larger due to misalignment between electrode 3 and the flow divergence angle δ.

T-O-F Velocity Probe Results

The effect of the time-of-flight current pulse on thruster operation is demonstrated in Fig. 16, which shows the arcjet current I_{arc} and voltage V_{arc} versus time during a typical pulse. The current drops suddenly as the FET switch closes (Fig. 7) and the 0.1 µF capacitor begins to charge. As the capacitor nears the end of the charge cycle (~ a few 1 µs R-C time constants), the current through the FET leg of the circuit decreases so that the arc current resumes the normal PPU ripple after a small positive ring. The width of the arcjet current deficit pulse is ~ 4 µs. The nature of the behavior of V_{arc} is not immediately clear from Fig. 16. However, the derivative of the arc current (dI_{arc}/dt) has the same qualitative behavior as V_{arc}, implying a possible inductive effect resulting from the arcjet geometry and/or from the current pulse circuitry.

The T-O-F probe response is shown in Fig. 17 for a typical centerline axial velocity measurement. The signal measured at the downstream electrode has been increased by a factor of 6 to account for the lower electron current (lower T_e and n_e) 5 mm downstream of the upstream electrode. Both the upstream and downstream electrodes show noise beginning at t ~ 2 µs that corresponds with the action of closing the FET switch. Approximately 3 µs later, the effect of the arcjet current pulse is monitored as a decrease in the electron current measured by the upstream electrode. After a time delay for the tagged flow to traverse the 5 mm electrode separation, a similar decrease is noted at the downstream electrode. For both of the signals, the width of the decrease in the measured electron current is ~ 4 µs, approximately the same as that of the current deficit pulse.

Axial velocities are inferred from the convective time delay demonstrated in Fig. 17 and the known separation (5.0 mm) between the two T-O-F electrodes. The time delays are derived from the probe response using the temporal separation between the minima (due to the decrease in electron current) measured at each electrode. This is accomplished by taking the derivative of each (smoothed) signal as shown in Fig. 18. The difference in the locations of the zero crossings is the time required for the tagged flow to travel the 5.0 mm electrode separation.

Results of T-O-F probe centerline velocity measurements are shown in Fig. 19 for data acquired during three individual periods after thruster ignition (cold start). The data show that the centerline axial velocity initially averages ~ 6.0 km/s during the period that the thruster is warming up. After approximately 5-7 minutes of run time, the axial velocity averages ~ 6.5 km/s. These data are consistent with our previous results[21] which indicate that exit plane n_e measurements reach steady state after ~ 4-8 minutes. During the warm-up period, the measured velocities fluctuate between 5.8 and 6.3 km/s. Similarly, the steady-state centerline axial velocities range from 6.3 to 6.7 km/s. These variations, although approximately within the experimental error, may be physical. Previous work utilizing CMV for a 1 kW hydrogen arcjet[26] has shown similar velocity fluctuations. In that work, it was determined that the phase of the PPU ripple was not responsible. Similarly, the arcjet current deficit pulse was always triggered at the same phase in the PPU current ripple (Fig. 16) for the data presented in this study. It is unclear what may be causing this phenomenon.

The T-O-F probe was also used for off-centerline measurements to generate an axial velocity profile at the thruster exit. For these data, an attempt was made to align the probe with the flow divergence angle δ. It was found that using a fixed angle (θ=0°) probe produced a flat or even inverted profile with a minima on the centerline. An off axis T-O-F probe that is grossly misaligned with the flow divergence angle (θ<<δ) will see a "faster" plasma at the downstream electrode than at the upstream electrode. Additionally, the electrode separation along the streamline is less than the geometric separation (5.0 mm) by the factor cos(δ). Both of these factors artificially increase the measured axial velocities, with the former phenomenon having a greater effect than the latter. Although the plasma streamlines are not known *a priori*, the error associated with

T-O-F probe misalignment for off axis measurements can be minimized by rotating the probe to align it with the expected flow divergence at a given location. The flow divergence has been shown[4] to be quite large ~ 10 mm from the thruster exit, and is expected to be large at the exit as well. For T-O-F measurements at r = 0, 1, 2, 3 and 4 mm, the probe angles used were $0°$, $10.8°$, $18.0°$, $25.2°$ and $45.0°$, respectively. It was assumed that velocities measured in this manner were along the probe angle and were converted to axial components.

Figure 20 shows the results of axial velocity measurements made at the thruster exit plane, with the upstream electrode located 1.0 mm from the exit. The profile is fairly symmetric and is compared with a computational model as discussed below.

Analysis of Crossed Probe Data

Since a measurement of the centerline value of the plasma velocity u_i has been made, quadruple probe data can be used to estimate the heavy particle kinetic temperature $T_g=T_i$. For the quadruple probe located at x=2.25 mm, the measured ratio of the ion currents collected by electrodes 3 and 4 is I_4/I_3 = 0.55 to 0.60. This current ratio, along with Fig. 4 for f=0.9 (κ=1.07), yields $u_i/c_{m,H^+}$ = 0.95 to 1.05, which indicates that the most probable thermal speed for H^+ (c_{m,H^+}) is approximately equal to the directed ion velocity u_i. For the measured centerline velocity u_i=6.5 km/s, the heavy particle temperature $[T_i=(c_{m,H^+})^2 m_{H^+}/2]$ is $T_g=T_i$ ~ 2500 K (0.2 eV). Therefore, with the previous results for T_e ~ 6700 K, the extent of thermal non-equilibrium on axis at the thruster exit is T_g/T_e ~ 0.4.

Since the perpendicular electrode P_4 in reality measures I_4 based on a distribution of u_i and T_i along its length, a discussion of the errors introduced by the probe size is in order. Because the quadruple probe theory for determining T_e and n_e uses the measured value of I_4/I_3, no error due to the presence of the perpendicular electrode is involved in determining T_e and n_e. This has been verified (above) with independent triple probe measurements. In interpreting the crossed probe data, however, the geometry of the probe becomes a factor. The current I_4 is likely slightly underrepresented due to changes in n_e and u_i along the electrode length. However, because $u_i/c_{m,H^+}$ is proportional to $1/(T_i)^{1/2}$, a T_i profile peaked at the centerline has the opposite effect on I_4. Assuming a 10% error in I_4, I_4/I_3= 1.1(0.57)~0.63. The ratio $u_i/c_{m,H^+}$ becomes ~ 1.15, and T_i becomes 2000 K (0.17 eV).

Comparison of Computational Model and Data

A computational arcjet modeling effort[30-31] has been undertaken by our group concurrent with the exit plane probe studies discussed above. The model is an axisymmetric, seven species hydrogen/nitrogen plasma code that utilizes a PISO algorithm to solve the computational domain up to the exit plane. Separate energy equations are formulated and solved for the electrons and the heavy species. The anode temperature distribution is included, and the plasma electrical conductivity is coupled with the plasma properties, which allows a self-consistent solution for the current distribution. The model is capable of both chemical equilibrium and non-equilibrium simulations. A complete discussion of the model and assumptions has been presented elsewhere.[30,31]

Comparisons are made between experimental results and model predictions for a 1 kW-class arcjet operating on 50 mg/s of $2H_2+N_2$ to simulate fully-decomposed hydrazine propellant. The arc current is 10.0 A for both model and experiment. The specific powers for the laboratory thruster (112 V, 10 A) and numerical model (94 V, 10A)

13

are 22.4 and 18.2 MJ/kg, respectively. The model specific power is contingent on the empirical value of the anode fall potential used. For the model results discussed below, a chemical non-equilibrium simulation is employed.

The centerline exit plane n_e predicted by the model is $n_e = 3 \times 10^{14}$ cm^{-3}, which, given the largely varying axial n_e gradients discussed above, seems consistent with previous experimental data (Fig. 13). Because of these large gradients, a direct comparison between the quadruple probe exit plane data (probe tip = 1 mm from exit) and the computational model is difficult.

Centerline exit plane heavy particle temperature predictions agree favorably with experiment ($T_{g,model} = 2800$ K, $T_{g,exp.} \sim 2000$-2500 K), but T_e results differ by a factor of ~ 2 ($T_{e,model} = 3000$ K, $T_{e,exp.} \sim 6600$ K). Based on experimental results of the present and previous studies, it thus appears that the numerical model may be underpredicting electron temperatures at the thruster exit plane. Note that model predictions of thrust, u_i, I_{sp} and T_g are unaffected, since the relative electron concentration is low ($n_e/n_n < 0.001$). Internal nozzle diagnostics[32] performed by our group are expected to help resolve the discrepancy between experiment and numerical model predictions.

Fig. 20 shows a comparison between the predicted axial velocity profile and the results of the T-O-F probe surveys. Agreement is excellent and within experimental error in most locations. The numerically predicted profile is slightly more narrow and peaked than the measured profile. This is an expected result because the model flow is constrained in the nozzle (no-slip at wall), which differs from the free expansion that occurs in the plume in the vicinity of the T-O-F probe.

VI. Summary and Conclusions

Experimental results for two electrostatic probe diagnostic techniques are presented for the very near-field plume of a 1 kW hydrazine arcjet. An improved quadruple probe theory, showing excellent agreement with independent triple probe surveys, was used to measure centerline axial profiles of T_e and n_e for x=2.25-6.25 mm from the exit plane. While the gradient in n_e is slight over the region investigated, indications are that the density varies by 1-2 orders of magnitude within the first few millimeters downstream of the exit plane. For the axial position nearest the thruster exit, T_e=6600 K, n_e=3.6 x 10^{12} cm^{-3} and $T_g = T_i \sim 2000$-2500 K. With the heavy particle temperature measurement, the extent of thermal non-equilibrium has been quantified at the thruster exit. A spatially resolved technique for measuring plasma axial velocities has also been developed and implemented. The radial velocity profile was measured at the exit plane, with a peak centerline velocity of 6500 m/s. The above results were used to evaluate the predictions of a numerical H_2/N_2 arcjet model. Agreement was very favorable for both the exit plane centerline T_g and radial u_i profile. Based on previous and current data, it appears that the model may underpredict exit plane T_e. Internal nozzle diagnostics are expected to illuminate the causes of this discrepancy. Comparison of n_e predictions and experimental data could not be attempted due to the large gradients in n_e present at the exit plane. Clearly, there are significant advances to be made in understanding fundamental arcjet physics, through both experimentation and modeling efforts.

VII. Acknowledgments

14

VIII. References

[1]Wilbur, P. J., Jahn, R. G., and Curran, F. C., "Space Electric Propulsion Plasmas," IEEE Transactions on Plasma Science, Vol. 19, No. 6, 1991, pp. 1167-1179.

[2]Carney, L. M. and Keith, T. G., "Langmuir Probe Measurements of an Arcjet Exhaust," *Journal of Propulsion and Power*, Vol. 5, No. 3, 1989, pp. 287-294.

[3]Carney, L. M. and Sankovic, J. M., "The Effects of Arcjet Operating Condition and Constrictor Geometry on the Plasma Plume," AIAA Paper 89-2723, July 1989.

[4]Sankovic, J. M., "Investigation of the Arcjet Plume Near Field Using Electrostatic Probes," NASA TM-103638, Nov. 1990.

[5]Sankovic, J. and Jankovsky, R., "An Experimental Investigation of the Effective Current Collecting Area of a Spherical Langmuir Probe in an Arcjet Thruster Exhaust," AIAA Paper 90-0073, Jan. 1990.

[6]Gallimore, A. D., Kim, S.-W., Foster, J. E., King, L. B., and Gulczinski, F. S., "Near and Far-field Plume studies of a 1 kW Arcjet," AIAA Paper 94-3137, June 1994.

[7]Langmuir, I. and Mott-Smith, H. M., "The Theory of Collectors in Gaseous Discharges," *Physical Review*, Vol. 28, 1926, pp.727-763.

[8]Chen, S.-L. and Sekiguchi, T., "Instantaneous Direct-Display System of Plasma Parameters by Means of Triple Probe," *Journal of Applied Physics*, Vol. 36, No. 8, 1965, pp. 2363-2375.

[9]Tilley, D. L., Kelley, A. J. and Jahn, R. G., "The Application of the Triple Probe Method to MPD Thruster Plumes," AIAA Paper 90-2667, July 1990.

[10]Gallimore, A. D., Kelley, A. J. and Jahn, R. G., "Anode Power Deposition in Quasisteady Magnetoplasmadynamic Thrusters," *Journal of Propulsion and Power*, Vol. 8, No. 6, 1992, pp. 1224-1231.

[11]Tilley, D. L., Gallimore, A. D., Kelley, A. J. and Jahn, R. G., "The Adverse Effect of Perpendicular Ion Drift Flow on Cylindrical Triple Probe Electron Temperature Measurements," *Rev. Sci. Instrum.*, Vol. 65, No. 3, 1994, pp. 678-681.

[12]Paccani, G., "Electrostatic Probe Diagnostics of Solid Propellant MPD Thruster Jets," AIAA Paper 94-3340, June 1994.

[13]Pobst, J. A., Schilling, J. H., Erwin, D. A. and Spores, R. A., "Time Resolved Measurements of 1 kW Arcjet Plumes using Current Modulation Velocimetry and Triple Langmuir Probes," International Electric Propulsion Conference Paper 93-128, Sept. 1993.

[14]Habiger, H. A., Auweter-Kurtz, M. and Kurtz, H., "Electrostatic Probes for the Investigation of Arc-Driven Electric Propulsion Devices," International Electric Propulsion Conference Paper 93-124, Sept. 1993.

[15]Kanal, M., "Theory of Current Collection of Moving Cylindrical Probes," *Journal of Applied Physics*, Vol. 35, No. 6, 1964, pp. 1697-1703.

[16]Bruce, C. and Talbot, L., "Cylindrical Electrostatic Probes at Angles of Incidence," *AIAA Journal*, Vol. 13, No. 9, 1975, pp. 1236-1238.

[17]Johnson, B. H. and Murphree, D. L., "Plasma Velocity Determination by Electrostatic Probes," *AIAA Journal*, Vol. 7, No. 10, 1969, pp. 2028-2030.

[18]Poissant, G. and Dudeck, M., "Velocity Profiles in a Rarefied Argon Plasma Stream by Crossed Electrostatic Probes," *Journal of Applied Physics*, Vol. 58, No. 5, 1985, pp. 1772-1779.

[19]Burton, R. L., DelMedico, S. G. and Andrews, J. C., "Application of a Quadruple Probe Technique to MPD Thruster Plume Measurements," *Journal of Propulsion and Power*, Vol. 9, No. 5, 1993, pp. 771-777.

[20]DelMedico, S. G., "Plasma Flow Measure-ments by a Quadruple Probe in a Quasi-Steady MPD Plasma," M.S. Thesis, University of Illinois, 1992.

[21]Burton, R. L., Bufton, S. A., Tiliakos, N. T. and Krier, H., "Application of Multiple Electrostatic Probes to a Low Power Arcjet," AIAA Paper 94-3299, June 1994.

[22]Omega CC High Temperature Cement and Binder, Omega Engineering, Inc., Stamford, CT.

[23]Chung, P. M., Talbot, L. and Touryan, K. J., <u>Electric Probes in Stationary and Flowing Plasmas: Theory and Application</u>, Springer-Verlag, 1975.

[24]Keefer, D., Moeller, T. and Rhodes, R., "Multiplexed Laser-Induced Fluorescence and Nonequilibrium Processes in Arcjets," AIAA Paper 94-2656, June 1994.

[25]Hargus, W., Micci, M. and Spores, R., "Interior Spectroscopic Investigation of the Propellant Energy Modes in an Arcjet Nozzle," AIAA Paper 94-3302, June 1994.

[26]Spores, R. A., Hargus, W. A., Pobst, J. A., Schilling, J. H., Lutfy, F. M. and Erwin, D. A., "Arcjet Diagnostics for Measuring Velocity, Density and Temperature," AIAA Paper 94-2464, June 1994.

[27]Curran, F. M. and Haag, T. W., "Extended Life and Performance Test of a Low-Power Arcjet," *Journal of Spacecraft and Rockets*, Vol. 29, No. 4, 1992, pp. 444-452.

[28]Zube, D. M., and Myers, R. M., "Nonequilibrium in a Low Power Arcjet Nozzle," AIAA Paper 91-2113, June 1991.

[29]Manzella, D. H., Curran, F. M., Myers, R. M. and Zube, D. M., "Preliminary Plume Characteristics of an Arcjet Thruster," AIAA Paper 90-2645, July 1990.

[30]Megli, T. W., Krier, H., Burton, R. L., and Mertogul, A., "Two-Temperature Modeling of N_2/H_2 Arcjets," AIAA Paper 94-2413, June 1994.

[31]Megli, T. W., Krier, H., and Burton, R. L., "A Plasmadynamics Model for Nonequilibrium Processes in N_2/H_2 Arcjets," AIAA Paper 94-1961, June 1995.

[32]Tiliakos, N. T., Burton, R. L. and Krier, H., "Application of Internal Langmuir Diagnostics for Arcjets," AIAA Paper 95-2386, July 1995.
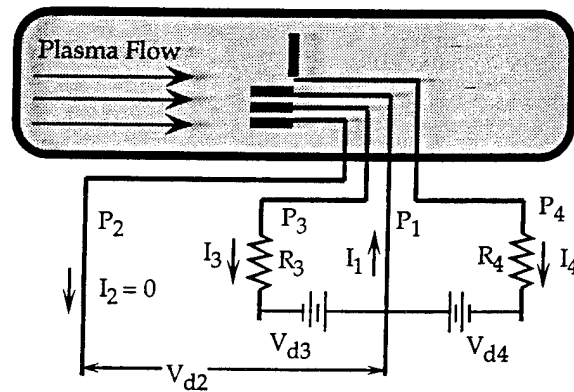
Fig. 1a. Quadruple probe electrical schematic. Measured quantities are V_{d2}, I_3 and I_4.
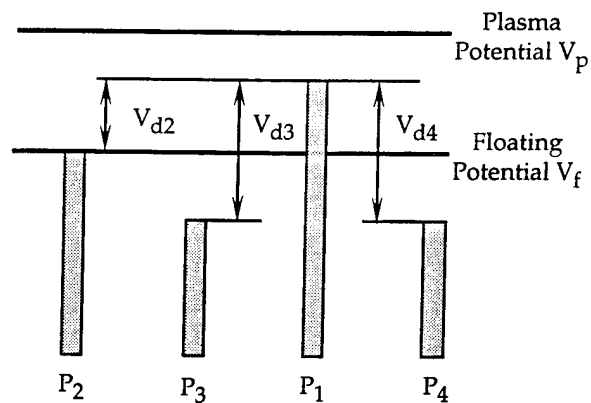
Fig. 1b. Quadruple probe electrode potential plot for $V_{d3}=V_{d4}$.
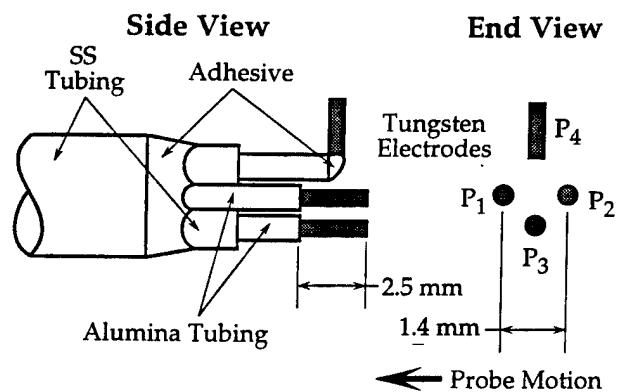
Fig. 2. Schematic of the quadruple probe tip swept through the arcjet plume.
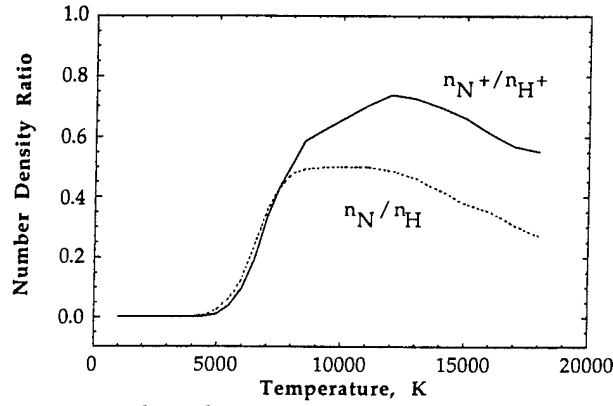
Fig. 3. Ionic and atomic number density ratios for simulated N_2H_4 at p=1 atm.
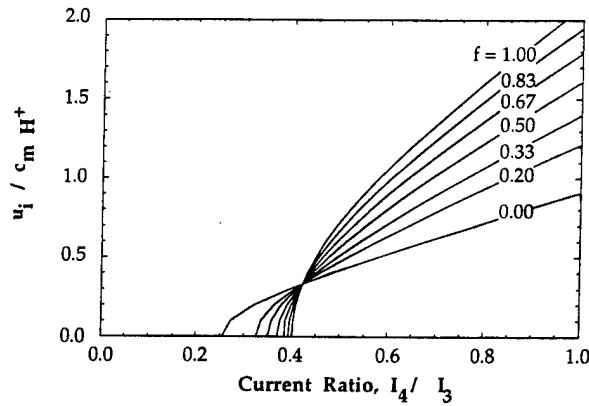
Fig. 4. Velocity ratio $u_i/c_{m,H^+}$ vs. I_4/I_3 for $0.0<f<1.0$. For this study, f (= n_{H^+}/n_e) ~ 0.9, corresponding to $\kappa=1.07$.
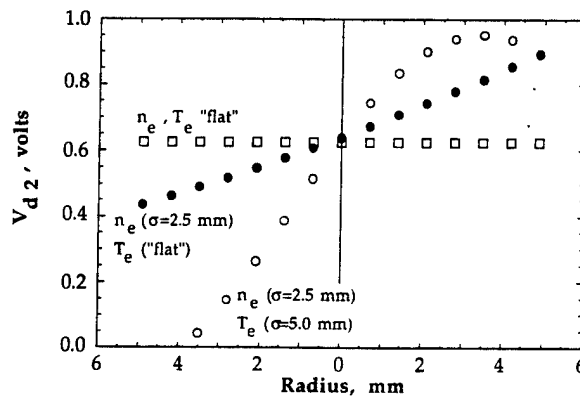

Fig. 5. Calculated quadruple probe response to axisymmetric Gaussian profiles of T_e and n_e with standard deviation σ (mm).
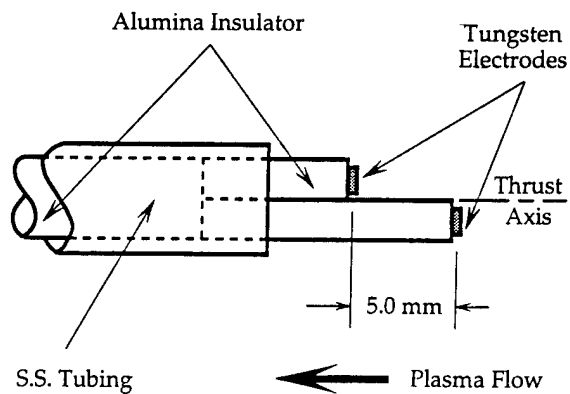
Fig. 6. Side view schematic of the time-of-flight electrostatic probe.
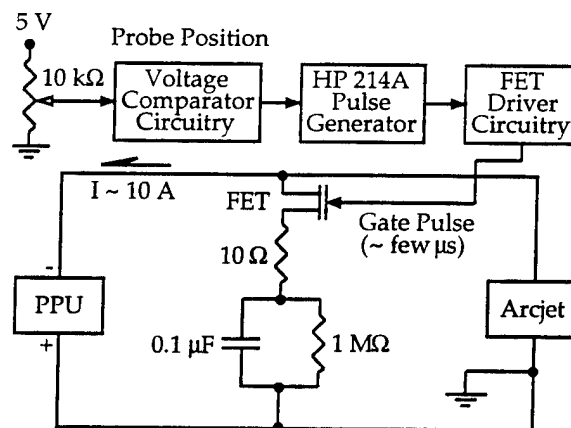
Fig. 7. Schematic of circuit used to trigger the arcjet current deficit pulse for T-O-F velocimetry.
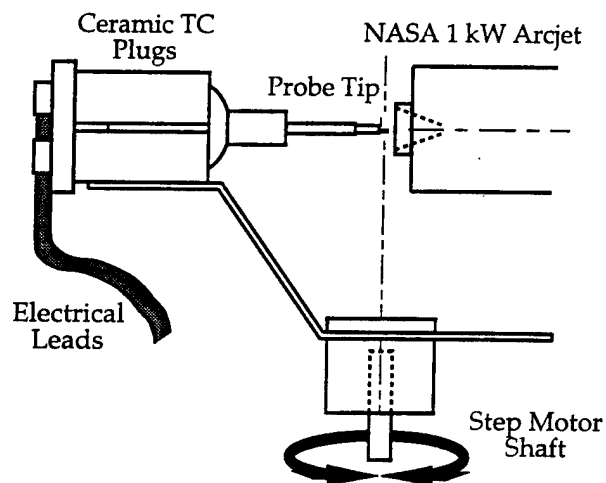
Fig. 8. Schematic of the probe mount. Probe axes can be rotated in 0.9° increments.
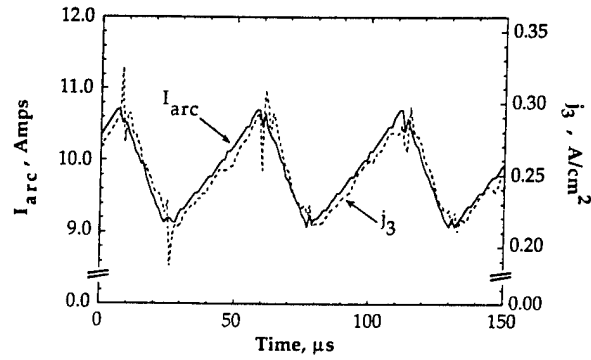
Fig. 9. Arcjet current and ion saturation current density showing the effects of the PPU ripple. The delay between I_{arc} and j_3 is ~ 3-4 µs.
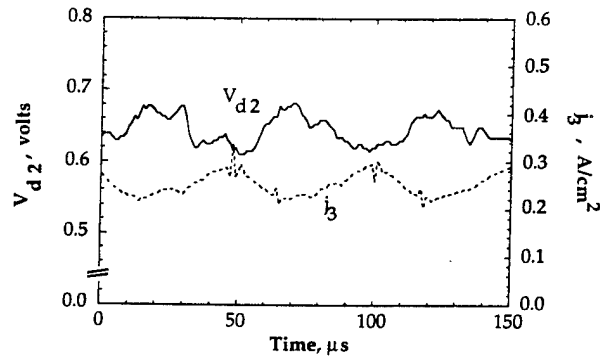
Fig. 10. V_{d2} and j_3 vs. time. Figs. 9 and 10 show that n_e increases and T_e decreases with increases in I_{arc}.
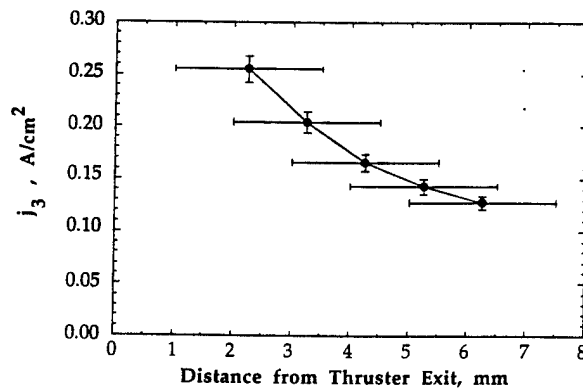
Fig. 11. Axial variation of the ion saturation current density. Horizontal error bars are 2.5 mm long, indicating the length of electrode 3.
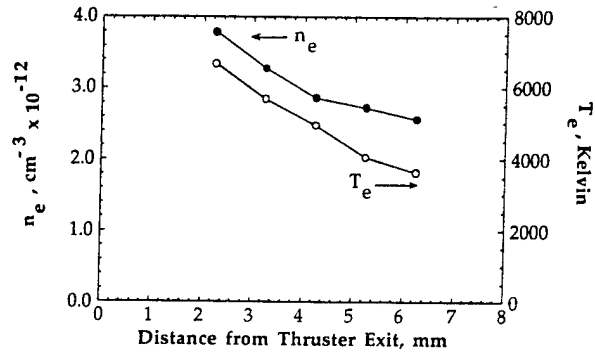
Fig. 12. Axial variation of T_e and n_e. The n_e gradient is ~ -0.5 x 10^{12} cm^{-3}/mm nearest the thruster. Experimental error in T_e is ± 15%.
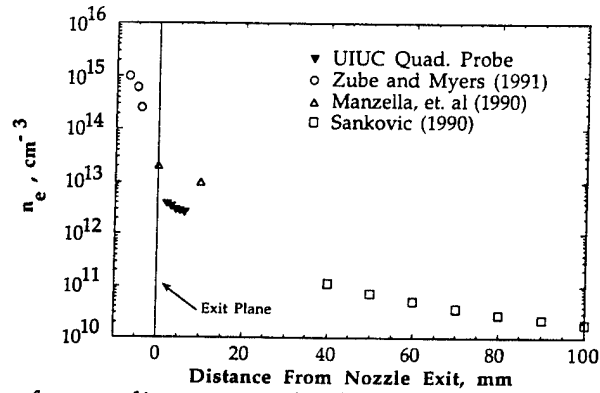
Fig. 13. Comparison of centerline n_e results from the present work and previous studies.
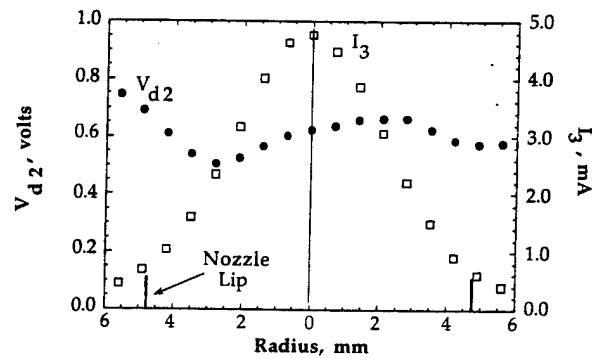
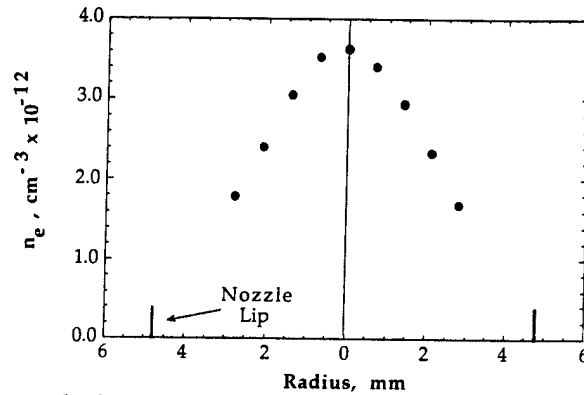Fig. 14. Smoothed profiles of $I_3(r)$ and $V_{d2}(r)$ measured by the quadruple probe.

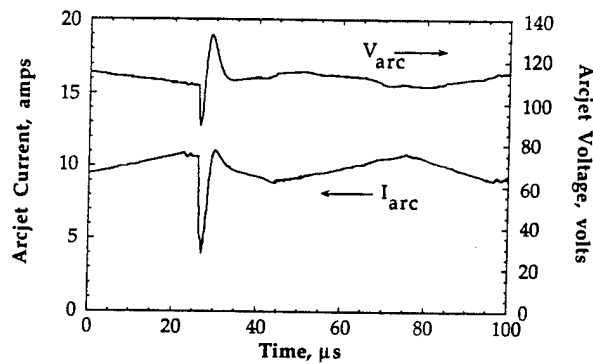Fig. 15. Measured n_e radial profile for x=2.25 mm from the thruster exit plane.

Fig. 16. Variation of I_{arc} and V_{arc} during the current deficit pulse. The pulse width is much smaller that the period of the PPU ripple.
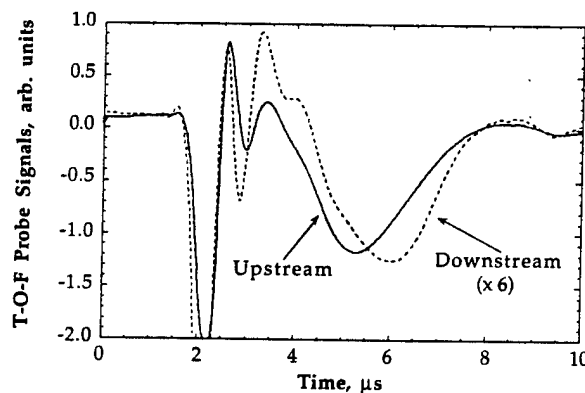

Fig. 17. Variation of the T-O-F probe signals during the current deficit pulse. Probe electrode signal delay is ~ 0.77 μs.
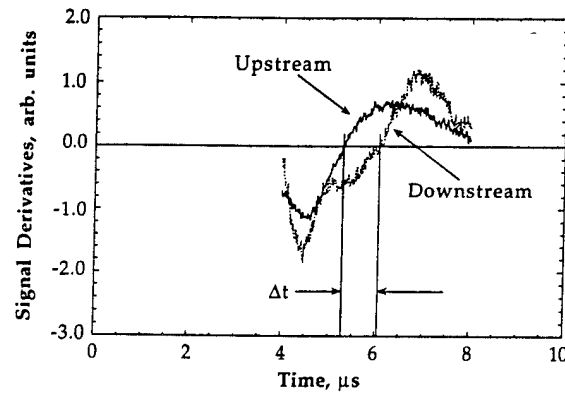
Fig. 18. Derivatives of the smoothed T-O-F probe signals depicting zero-crossings at signal minima locations.
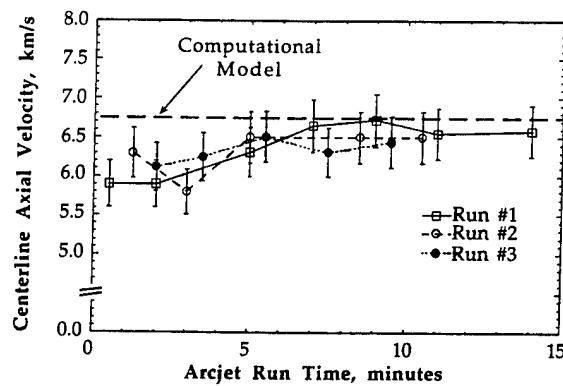

Fig. 19. Measured centerline axial velocity vs. time for arcjet warm-up. The numerical model prediction is also shown.
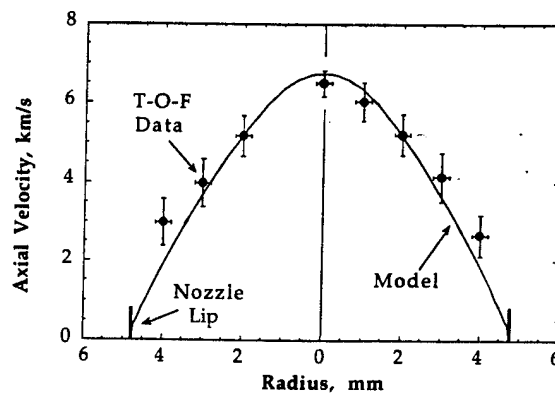

Fig. 20. Experimental measurements and model predictions of the axial velocity profile at the thruster exit.

A PLASMADYNAMICS MODEL FOR NONEQUILIBRIUM PROCESSES IN N$_2$/H$_2$ ARCJETS

Abstract

A general, two-dimensional, steady, non-LTE (local thermodynamic equilibrium) model is presented for nitrogen/hydrogen arcjet thrusters. Both thermal and chemical nonequilibrium processes are incorporated to describe a multi-temperature, multi-species N$_2$/H$_2$ plasma. The current and anode temperature distributions are fully coupled to the plasma flowfield with realistic boundary conditions. Thermal nonequilibrium, chemical equilibrium results are presented for simulated hydrazine. Results for both thermal and chemical nonequilibrium hydrazine and hydrogen arcjets show significant thermal nonequilibrium near the anode, and high frozen flow losses. It is concluded that nonequilibrium chemistry models are necessary to capture accurately the interior distributions of the plasma flowfield.

Nomenclature

c_i mean thermal speed (m/s)
C   coulomb charge
D_i effective diffusion coefficient (m^2/s)
elst   elastic energy transfer (W/m^3)
g_0 gravitational acceleration at sea level (m/s^2)
h   Planck's constant (J-s)
h_i enthalpy of species i (J/kg)
H   heavy species total particle energy (J)
I   integrated total current (A)
I_{sp} specific impulse (s)
j   current density (A/m^2)
k_b Boltzmann's constant (J/K)
k_c Coulomb constant (Nm^2/C^2)
k_f Forward rate coefficient (m^6/s or m^3/s)
k_r Reverse rate coefficient (m^6/s or m^3/s)
L_e Electron inelastic loss rate (W/m^3)
L_h Heavy species inelastic loss rate (W/m^3)
m_i mass of species i (kg)
m_{ij} reduced mass (kg)
$\dot{m}$ mass flow rate (kg/s)
M   Mach number
n_i number density of ith species (m^{-3})
p   pressure (N/m^2)
P_Ω integrated ohmic power deposition (W)
Q_{ij} collision cross section (m^2)
T_a anode temperature (K)
T_e electron temperature (K)
T_g heavy species temperature (K)
T   thrust (N)
u   axial velocity (m/s)
v   radial velocity (m/s)
v   velocity vector (m/s)
V   voltage (volts)
w   azimuthal swirl velocity (m/s)
x,r,θ cylindrical coordinates
x_i mole fraction of species i
y_i mass fraction of species i

x_{con}	constrictor length (mm)
x_{mol}	mixture parameter in $x_{mol} N_2 + H_2$
Z_i	thermodynamic partition functions
α_i	catalytic efficiency of species i
ε_d	dissociation energy (J)
ε_i	ionization energy (J)
ε	anode emissivity
λ_a	anode thermal conductivity (W/m-K)
λ_e	electron thermal conductivity (W/m-K)
λ_h	heavy species thermal conductivity (W/m-K)
Λ_e	Spitzer logarithm term
μ	gas viscosity (kg/m-s)
ν	collision frequency (s^{-1})
θ_{vH2}	H_2 vibrational temperature (K)
θ_{vN2}	N_2 vibrational temperature (K)
ρ	mass density (kg/m^3)
σ	electrical conductivity (mhos/m)
$\underline{\tau}$	stress tensor (N/m^2)
Ω_{ij}	collision integral (m^2)

I. Introduction

Electrothermal arcjets offer a significant advantage in specific impulse and cost over conventional satellite propulsion systems. Low power 1-2 kW systems have been flight qualified and are now used for north-south station keeping, while higher power 20-30 kW designs are in advanced development for orbit transfer applications.[1]

The arcjet is shown schematically in Fig. 1. The fluid dynamics and energy transfer within the arcjet thruster are nonlinear and strongly coupled. The propellant is injected upstream of the constrictor, typically with an azimuthal (or 'swirl') velocity component. The energy conversion mechanism for an arcjet is an arc discharge, produced by a voltage difference between the thruster nozzle, which is the anode, and a conical cathode on the upstream side of the constrictor. Typical operating voltages for 1 kW class arcjets are 100 V DC at a current of I = 10 A. The arc current distribution depends on several factors in addition to the geometry. The distribution is coupled to the propellant mass flow rate, composition, thermal properties, electrical conductivity, and gas-dynamic properties.

Both chemical and thermal processes in the arcjet are described as nonequilibrium. Arc current is converted to electron thermal energy through ohmic dissipation. The electrons transfer thermal energy to heavy species in the arc plasma through collisions. This energy is then converted to thrust as the fluid accelerates through the nozzle. In regions of low pressure and/or elevated ohmic heating, collisional coupling between electrons and heavy species may not establish equal gas and electron temperatures. Additionally, flow velocities are large so that fluid residence times in the nozzle are of the order of a few μs; much of the energy invested in dissociation and ionization is frozen. Pressures drop from roughly 1 atm at the constrictor to millitorr conditions at the exit; radial diffusion of electrons from the arc core is important in determining the arc structure.

The thrust and specific impulse produced by an arcjet are determined by several factors including the power transferred to the propellant, the extent of both kinetic and chemical nonequilibrium, the propellant gas mixture, and the arcjet nozzle geometry. Other factors which contribute to the overall performance include the thermal loading of the anode,[2] and the voltage sheaths at the electrodes. A comprehensive model of an arcjet thruster is highly complex, including plasmadynamic, fluid dynamic, radiative, and surface and volumetric heat transfer phenomena.

Most arcjet design strategies to date have been empirical, with design improvements based on experimental observations. The need for a more complete description of the complex physical processes has resulted in a variety of numerical efforts ranging from simplified one-dimensional models[3-8] to more comprehensive two-dimensional descriptions of the gas dynamics and energy transfer processes.[9-22] Comprehensive arcjet models are required to (1) interpret experimental results, (2) understand the physical processes in regions of the thruster

where diagnostic techniques are challenging, (3) improve arcjet performance and (4) scale the devices to higher or lower power levels.

II. Nonequilibrium Model

An axisymmetric, steady, laminar, continuum flow, two-temperature kinetic nonequilibrium model is formulated for a direct current arcjet with flow swirl, a variable nozzle geometry, and a variable mixture ratio of nitrogen and hydrogen. Flow swirl is modeled by including an azimuthal momentum equation. Two methods are used to determine species populations. If chemical equilibrium is assumed, the species populations are computed from a generalized law of mass action. For chemical nonequilibrium simulations, populations are determined from species continuity equations.

The model predicts thrust, specific impulse, and internal fields for pressure p, mass density ρ, seven species densities n_i, and anode T_a, electron T_e and heavy species T_g temperatures. Additionally, the model predicts the current density distribution $\mathbf{j}$, voltage potential V, and velocity components u, v, and w.

The details of the model are presented in six sections below as: (1) the fluid dynamic equations, (2) the energy equations, (3) the electromagnetic equations, (4) the species number density equations, (5) transport coefficients, and (6) boundary conditions. The arcjet geometry is described as (x,r,θ) where x is the axial coordinate, r is the radial coordinate, and θ is the azimuthal coordinate.

<u>1. Fluid Dynamic Equations</u>

The viscous fluid dynamic equations are summarized below:

Axial momentum:

$$\frac{\partial(\rho uu)}{\partial x} + \frac{1}{r}\frac{\partial(r\rho uv)}{\partial r} = \frac{4}{3}\frac{\partial}{\partial x}\left(\mu\frac{\partial u}{\partial x}\right) + \frac{1}{r}\frac{\partial}{\partial r}\left(\mu r\frac{\partial u}{\partial r}\right)$$
$$- \frac{2}{3}\frac{\partial}{\partial x}\left(\mu\frac{\partial v}{\partial r}\right) - \frac{2}{3r}\frac{\partial(\mu v)}{\partial x} + \frac{1}{r}\frac{\partial}{\partial r}\left(\mu r\frac{\partial v}{\partial x}\right) - \frac{\partial p}{\partial x}$$

(1)

Radial momentum:

$$\frac{\partial(\rho uv)}{\partial x} + \frac{1}{r}\frac{\partial(r\rho vv)}{\partial r} = \frac{\partial}{\partial x}\left(\mu\frac{\partial v}{\partial x}\right) + \frac{4}{3r}\frac{\partial}{\partial r}\left(\mu r\frac{\partial v}{\partial r}\right)$$
$$+ \frac{\partial}{\partial x}\left(\mu\frac{\partial u}{\partial r}\right) + \frac{2\mu}{3r}\frac{\partial u}{\partial x} - \frac{2v}{3r}\frac{\partial\mu}{\partial r} - \frac{4}{3}\frac{\mu v}{r^2}$$
$$- \frac{2}{3r}\frac{\partial}{\partial r}\left(\mu r\frac{\partial u}{\partial x}\right) - \frac{\partial p}{\partial r} + \frac{\rho w^2}{r}$$

(2)

Azimuthal momentum $(\partial p/\partial\theta = 0)$:

$$\frac{\partial(\rho u(wr))}{\partial x} + \frac{1}{r}\frac{\partial}{\partial r}((r\rho v + 2\mu)(wr)) =$$
$$\frac{\partial}{\partial x}\left(\mu\frac{\partial(wr)}{\partial x}\right) + \frac{1}{r}\frac{\partial}{\partial r}\left(\mu r\frac{\partial(wr)}{\partial r}\right)$$

(3)

26

Axisymmetric continuity:

$$\frac{\partial}{\partial x}(\rho u) + \frac{1}{r}\frac{\partial}{\partial r}(r\rho v) = 0 \qquad (4)$$

2. Energy Equations

The assumption of kinetic nonequilibrium gives separate energy equations for the electrons and heavy species. For the chemical equilibrium model, the electron energy equation is:

$$\nabla \cdot \left(\left(n_e v - \frac{j}{e} \right)\left(C_{pe}T_e \right) \right) = \nabla \cdot \left(\lambda_e \nabla T_e \right)$$
$$+ \nabla \cdot \left(\frac{1}{m_e}\rho C_{pe}T_e D_e \nabla y_e \right) + \frac{j \cdot j}{\sigma} - \text{elst} - \text{radiation} \qquad (5)$$

where 'elst' represents energy lost through elastic collisions with the heavy species,[23] and 'radiation' denotes optically thin radiation loss due to continuum bremsstrahlung.[24] The elastic energy transfer source term is calculated as the sum of electron-molecule, -atom, and -ion contributions as:

$$\text{elst} = 3k_b(T_e - T_g)n_e m_e \sum_{i \neq e} \frac{\overline{v}_{ei}}{m_i} \qquad (6)$$

where the average collision frequencies $\overline{v}_{ei}$ between electrons and heavy species are calculated using the mean electron thermal speed and collision cross sections Q_{es} as:[24]

$$\overline{v}_{es} = \sqrt{\frac{8k_bT_e}{\pi m_e}}\, n_s Q_{es} \qquad (7)$$

where the electron-ion cross sections are:

$$Q_{ei} = \frac{\pi e^4 k_c^2 \ln\Lambda_e}{2(k_b T_e)^2} \qquad (8)$$

Electron-molecule collision frequencies are multiplied by an energy loss factor δ to account for inelastic losses to the internal energy modes.[8, 25] A constant loss factor of $\delta = 3000$, chosen for the simulations presented here, is discussed below.

The chemical equilibrium energy equation for heavy species (molecules, atoms, and ions) is:

$$\nabla \cdot (n_h v H) = \nabla \cdot (\lambda_h \nabla T_g) +$$
$$\sum_{i \neq e} \frac{1}{m_i}\nabla \cdot \left(\rho(C_{pi}T_g + h_i^0) D_i \nabla y_i \right) + \text{elst} + \nabla \cdot (v \cdot \tau) \qquad (9)$$

where

$$H = \frac{1}{n_h} \sum_{i \neq e} \left(n_i \left(C_{pi}T_g + h_i^0 + \frac{m_i v \cdot v}{2} \right) \right) \qquad (10)$$

The ionization and dissociation energies of molecules and atoms are arbitrarily included in the heavy species energy equation as reference enthalpies h_i^0. The reference enthalpies and specific heats are summarized in Table 1.

For chemical nonequilibrium simulations, a finite rate chemistry model is used to determine inelastic energy exchange rates between the particle classes. This model is summarized in Table 2, which lists the individual reaction rates and energy exchanges assumed for each chemical process.[26-29] The species continuity equations are multiplied by the reference enthalpies associated with each chemical reaction, and the terms appearing in the energy equations as the

convection and diffusion of ionization and dissociation potentials are replaced with energy transfer rates. The electron energy equation for chemical nonequilibrium is then

$$\nabla \cdot \left(\left(n_e v - \frac{j}{e} \right) \left(C_{pe} T_e \right) \right) = \nabla \cdot (\lambda_e \nabla T_e)$$
$$+ \nabla \cdot \left(\frac{1}{m_e} \rho C_{pe} T_e D_e \nabla y_e \right) + \frac{j \cdot j}{\sigma} - \text{elst} - \text{radiation} - \sum L_e \tag{11}$$

where individual energy loss rates L_e are summarized in Table 2.

The chemical nonequilibrium heavy species energy equation is:

$$\nabla \cdot (n_h v H) = \nabla \cdot (\lambda_h \nabla T_g) + \sum_{i \neq e} \frac{1}{m_i} \nabla \cdot (\rho C_{pi} T_g \, D_i \nabla y_i)$$
$$+ \text{elst} + \nabla \cdot (v \cdot \tau) - \sum L_h \tag{12}$$

where the total energy is now:

$$H = \frac{1}{n_h} \sum_{i \neq e} \left(n_i \left(C_{pi} T_g + \frac{m_i v \cdot v}{2} \right) \right) \tag{13}$$

The anode temperature distribution is determined from the energy equation for heat conduction in a solid. Neglecting ohmic dissipation in the anode gives

$$\nabla \cdot (\lambda_a \nabla T_a) = 0 \tag{14}$$

where $\lambda_a = \lambda_a(T_a)$.[30]

3. Species Equations

For chemical equilibrium (CE) simulations, the species number densities are given as a function of the pressure p, the heavy species temperature T_g, and the electron temperature T_e. A seven-species plasma composition of N_2, H_2, N, H, N^+, H^+, and electrons is assumed. Dissociation and ionization equations are constructed from a generalized law of mass action as given by entropy maximization.[31] This yields the following equations for the nitrogen and hydrogen species:

$$\frac{n_H^2}{n_{H_2}} = \exp\left(\frac{-\varepsilon_{d,H_2}}{k_b T_g} \right) \left(\frac{\pi m_H k_b T_g}{h^2} \right)^{3/2}$$
$$\times \left(\frac{Z_{H,ex}^2}{Z_{H_2,ex} Z_{H_2,rot} Z_{H_2,vib}} \right) . \tag{15a}$$

$$\frac{n_N^2}{n_{N_2}} = \exp\left(\frac{-\varepsilon_{d,N_2}}{k_b T_g} \right) \left(\frac{\pi m_N k_b T_g}{h^2} \right)^{3/2}$$
$$\times \left(\frac{Z_{N,ex}^2}{Z_{N_2,ex} Z_{N_2,rot} Z_{N_2,vib}} \right) \tag{15b}$$

$$\frac{n_e n_{H^+}}{n_H} = 2 \exp\left(\frac{-\varepsilon_{i,H}}{k_b T_e} \right) \left(\frac{2\pi m_e k_b T_e}{h^2} \right)^{3/2} \left(\frac{Z_{H^+,ex}}{Z_{H,ex}} \right) \tag{15c}$$

$$\frac{n_e n_{N+}}{n_N} = 2\exp\left(\frac{-\varepsilon_{i,N}}{k_b T_e}\right)\left(\frac{2\pi m_e k_b T_e}{h^2}\right)^{3/2}\left(\frac{Z_{N+,ex}}{Z_{N,ex}}\right) \tag{15d}$$

In the above expressions, the excitation partition functions Z_{ex} are functions of T_e, while Z_{rot} and Z_{vib} are functions of T_g. Details for the calculation of the various partition functions can be found in References 24 and 31-34.

The plasma equation of state, quasi-neutrality, and the definition of the mixture parameter x_{mol} provide the additional relations required to solve for the seven unknown species. Note that the initial mixture composition is written as $x_{mol}N_2 + H_2$ so that pure hydrogen ($x_{mol} = 0$), simulated hydrazine ($x_{mol} = 1/2$) and simulated ammonia ($x_{mol} = 1/3$) can be easily investigated:

$$x_{mol} = \frac{2n_{N_2} + n_N + n_{N+}}{2n_{H_2} + n_H + n_{H+}} \tag{16}$$

$$n_e = n_{H+} + n_{N+} \tag{17}$$

$$p = n_e k_b T_e + (n_{N_2} + n_{H_2} + n_N + n_H + n_e)k_b T_g \tag{18}$$

For chemical nonequilibrium (CNE) simulations, Eqs. (15) and (16) are replaced by individual species continuity equations, which are written in terms of the species mass fractions $y_i = m_i n_i/\rho$:

$$\nabla\cdot(\rho v y_i) = \nabla\cdot(\rho D_i \nabla y_i) + \dot{\rho}_i \tag{19}$$

Mixture-averaged mass diffusion coefficients D_i are employed, rather than multi-component diffusion coefficients. With this method, Eq. (19) is solved for y_{N_2}, y_H, y_N, y_{N+}, and y_{H+}. The electron population is then calculated from Eq. (17), and y_{H_2} is determined from overall mass continuity, or equivalently $\Sigma y_i = 1$. The species productions rates, $\dot{\rho}_i = m_i \dot{n}_i$, are determined as a function of T_g and T_e from the finite-rate chemistry processes summarized in Table 2. The references for the individual reaction rates are summarized in the right column of Table 2. For two-way reactions, the reverse reaction rates are extracted from the forward reaction rate and the 'equilibrium constants' given by Eqs. (15a-d).

4. Electromagnetic Equations

The calculation of the electrical current distribution is critical to understanding arc physics and poses a challenging problem in arcjet analysis. The current distribution is largely determined by the flow-field electrical conductivity σ, which is a strong function of the electron number density and temperature distribution. Models which assume local thermodynamic equilibrium (LTE) must artificially elevate σ in the cool boundary layer region to avoid excessive voltage drops near the anode.[11,15] The artificial restriction that $T_e = T_g$ results in an underprediction in the ionization (and therefore electron number density and σ) in the boundary layer regions and a subsequent overprediction in power deposition. Hence, the 'conductivity floor' is employed elsewhere[10,14] to provide agreement between the experimentally-observed and predicted power depositions.

Diffusion of electrons from the arc core towards the anode wall also elevates the electron number density and plays an important role in determining the boundary layer electrical conductivity. This has been demonstrated by Butler, Kull, and King,[11] who show that the incorporation of mass diffusion provides a reasonable current distribution without imposing artificial restrictions on σ or the current attachment region. However, the two-temperature solutions of Miller and Martinez-Sanchez[17] and Keefer et al.[16] demonstrate that significant kinetic nonequilibrium, with elevated T_e, exists outside of the arc core in the constrictor region. These results indicate that both diffusion and increased ionization due to elevated T_e are important factors which determine the boundary layer electrical conductivity.

The correct approach to the arc attachment problem is to model the anode as an equipotential surface and allow the current distribution to be a model output which is independent of artificial restrictions. This is a self-consistent approach to solving for the current distribution and electric field simultaneously, for which the current distribution is properly coupled to the flow-field.

Assuming induced magnetic fields are negligible, and neglecting electron pressure gradient driving terms, Ohm's law and current conservation are used to solve for $\mathbf{j}$ and V:[25]

$$-\nabla V = \mathbf{j}/\sigma \tag{20}$$

$$\nabla \cdot \mathbf{j} = 0 \tag{21}$$

5. Transport Coefficients

Transport coefficients for this model are calculated using mean free path mixture rules.[35] The viscosity is computed as:

$$\mu = \sum_{i=1}^{N} \frac{n_i}{\sum\limits_{j=1}^{N} n_j M_{ij}} \mu_i \tag{22}$$

where M_{ij} is defined as

$$M_{ij} = \sqrt{\frac{2m_{ij}}{m_i}} \frac{\overline{\Omega}_{ij}^{(2,2)}}{\overline{\Omega}_{ii}^{(2,2)}} \tag{23}$$

and the pure species viscosity is

$$\mu_i = 1/2 m_i n_i c_i l_i \tag{24}$$

where c_i is the mean thermal speed, l_i is the mean free path, and $\overline{\Omega}_{ij}$ is the energy-averaged collision integral for interaction between species i and j.

The translational contribution to the heavy species thermal conductivity is calculated using an equation similar to (24) with the pure species conductivity given as:

$$\lambda_i = \frac{15}{8} k_b n_i c_i l_i \left(\frac{9\gamma_i - 5}{15\gamma_i - 15} \right) \tag{25}$$

The electron thermal conductivity is:

$$\lambda_e = \frac{\frac{15}{8} k_b n_e^2 c_e l_e \left(\frac{9\gamma_e - 5}{15\gamma_e - 15} \right)}{\sum\limits_{j=1}^{N} n_j M_{ij}} \tag{26}$$

and electrical conductivity is calculated from:

$$\sigma = \frac{n_e e^2}{m_e \sum_{i \neq e} n_i c_e \overline{\Omega}_{e\text{-}i}^{(1,1)}} \qquad (27)$$

The effective diffusion coefficients D_i are calculated from:

$$D_i = \frac{1 - x_i}{\sum_{j \neq i} x_j/D_{ij}} \qquad (28)$$

where the D_{ij} are the binary mixture diffusion coefficients given as:[36]

$$D_{ij} = \frac{3}{16n\overline{\Omega}_{ij}^{(1,1)}} \left(\frac{2k_b T(m_i + m_j)}{\pi m_i m_j} \right)^{1/2} \qquad (29)$$

The electron and ion diffusion coefficients are modified to account for the ambipolar electric field. Assuming $\frac{\nabla n_e}{n_e} \approx \frac{\nabla n_{H+}}{n_{H+}} \approx \frac{\nabla n_{N+}}{n_{N+}}$, the ambipolar diffusion coefficients for electrons, H^+, and N^+ are:

$$D_{a,e} = \frac{D_e(\mu_{H+} n_{H+} + \mu_{N+} n_{N+}) + \mu_e (D_{H+} n_{H+} + D_{N+} n_{N+})}{\mu_e n_e + \mu_{H+} n_{H+} + \mu_{N+} n_{N+}} \qquad (30)$$

$$D_{a,H+} = \frac{D_{H+}(\mu_e n_e + \mu_{N+} n_{N+}) + \mu_{H+} (D_e n_e - D_{N+} n_{N+})}{\mu_e n_e + \mu_{H+} n_{H+} + \mu_{N+} n_{N+}} \qquad (31)$$

$$D_{a,N+} = \frac{D_{N+}(\mu_e n_e + \mu_{H+} n_{H+}) + \mu_{N+} (D_e n_e - D_{H+} n_{H+})}{\mu_e n_e + \mu_{H+} n_{H+} + \mu_{N+} n_{N+}} \qquad (32)$$

where the mobilities μ are calculated from $\mu_i = \frac{eD_i}{T_i}$.

The above relations require the energy-averaged collision integrals for 28 species interactions. Collision integrals and collision cross sections are obtained from References 37-43. Temperature-dependent curve fits are used for the transport property and elastic transfer calculations.

6. Boundary Conditions

The physical boundary conditions for the continuity, momentum, energy, and electromagnetic equations are summarized in Table 3 and Fig. 1. At the inflow boundary 1A, the flow is axial and the total temperature T_t and total pressure p_t are specified. The total pressure is adjusted to obtain the desired mass flow rate. The u-velocities and the inlet static temperatures are then computed from the isentropic stagnation property relations. The effects of flow swirl are incorporated by specifying the azimuthal inlet w-velocities as a fraction of the u-velocities. At the solid cathode 1C and anode 1D surfaces, no-slip conditions are employed. Zero radial gradients are specified on the center-line 1E.

31

At the outflow boundary 1B, the static pressure is extrapolated from the interior of the flow. The outflow u-velocities are updated to satisfy continuity using velocity corrections as given by discretized forms of the momentum and continuity equations for the exit plane. This is consistent with the numerical solution method discussed in section III below. Note that a zero electron temperature gradient is employed at the walls 1C and 1D. At low temperatures, the electron thermal conductivity approaches zero so that this boundary condition will have little effect on the results.[44]

The boundary conditions for the voltage are shown in Table 3. The anode is modeled as an equipotential surface, while the cathode voltage is equipotential with the voltage updated to obtain the specified total current I. Note that in this formulation the electrode sheath voltage drops V_s have been uncoupled from the bulk plasma. The axial gradient of the voltage is set to zero at the inflow and outflow boundaries so that current is forced to attach within the arcjet nozzle. Recent radial electric field and σ measurements along the exit plane, showing the existence of roughly 1 A/cm^2 current density, suggest that this boundary condition may need refinement.[45]

The boundary conditions for the anode energy equation are also shown in Table 3. On the outer surfaces 2B and 2D, the local heat flux is given by radiation to the surroundings at a specified background temperature $T_{bg} << T_a$ and a constant emissivity of $\varepsilon = 0.31$. Along the anode surface 2C, the net heat flux is calculated as the sum of (1) the heat flux due to conduction and species diffusion from the flow-field, (2) the radiation loss through the exit plane to the surroundings, and (3) the sheath losses given by the product of the local current density and an assumed sheath voltage drop $V_s = 13$ V. Note that radiation exchange between the plasma and the anode is neglected in this formulation. The upstream anode surface 2A is either a fixed temperature or zero heat flux boundary.

The chemical nonequilibrium model requires boundary conditions for the species populations. At the anode surface, the diffusion velocities are equated to a fraction α_i of the species thermal velocities:[29]

$$D_i \frac{\partial y_i}{\partial n} = \frac{\alpha_i}{4} \sqrt{\frac{8 k_b T_g}{\pi m_i}} \tag{33}$$

The anode is assumed to be catalytic for recombination, so that $\alpha_{H+} = \alpha_{N+} = \alpha_H = \alpha_N = 1$. Assuming that molecules are reflected from the surface gives $\alpha_{H2} = \alpha_{N2} = 0$. The inflow is in chemical equilibrium up to the constrictor entrance, where the chemical nonequilibrium simulation begins. The mass fractions at the exit plane are extrapolated from the interior of the flow.

III. Numerical Solution Method

The solution method is structured around the global continuity and momentum equations. These are solved using a compressible form of the pressure-based PISO algorithm,[46] where the density variations are implicitly included in the pressure-correction procedure as described by Rhie.[47] Staggered velocity and scalar grids yield a well-connected pressure field. Upstream weighted densities are employed to insure numerical stability.[48] The equations are discretized over finite cell volumes, and power law differencing of convective and diffusive portions of the linearized coefficients preserves numerical stability in regions of the flow where convection dominates. The solution process is iterative, and values for the field variables from the latest iteration are used to linearize the source terms. Under-relaxation is employed so that updated solutions are fractionally added to the solution from the previous iteration. The governing equations are transformed into natural coordinates and solved on a uniform computational mesh.

Figure 2 illustrates the solution algorithm. The energy equations are solved to update gas, electron, and anode temperature fields. The species number densities, transport coefficients, and source terms are then updated using the latest available temperatures and pressures. The continuity and momentum equations are solved to

update the pressure and velocity fields. Finally, the voltage and current density distributions are updated. Iterations are continued until (1) the normalized energy equation residuals are within 1% of the electrical power input, (2) the difference between the inlet and exit plane mass flow rates is less than 1% of the total mass flow rate, and (3) the axial and radial momentum equation residuals are within 1% of their respective exit momentum fluxes.

IV. Results and Discussion

Overview of Previous Simulations

Before proceeding to the present results, a discussion of the effect of the electron-molecule inelastic loss factor δ on our initial voltage predictions is appropriate. For the NASA-Lewis 1 kW arcjet geometry, we found that the δ-factors quoted in Ref. 25 ($\delta \approx O(10\text{-}100)$) resulted in current attachment in the constrictor, with corresponding underpredictions of the operating voltage of $V \approx 40$ V at $I = 10$ A. We also noted that increasing the mass flow rate had little or no effect on the attachment location. We electrically insulated the constrictor and observed little effect on the voltage prediction. Martinez-Sanchez recently re-examined the δ-factors for N_2, and values as high as $\delta \approx 4000$ were noted.[8] We choose $\delta = 3000$ because (1) reasonable convective effects result, with the arc being swept further downstream as the mass flow rate is increased, as was originally postulated in Ref. 8, and (2) better agreement is achieved between the predicted and experimentally observed operating voltage, while maintaining the equipotential anode voltage boundary condition in the constrictor.

The constrictor has been electrically insulated by others to provide better agreement between measured and predicted voltage.[16,17] These models simulated the German TT1 thruster, a higher power 10 kW arcjet with an ≈ 5 mm long constrictor, and predicted that nearly all of the electrical power was deposited in the constrictor. The predictions for our geometry, where $x_{con} = 0.25$ mm, indicate that roughly 50% of the power is deposited downstream of the constrictor.

Results

We present three simulations for the geometry of a NASA-Lewis 1 kW arcjet. These are summarized in Table 4, where mass flow rate, voltage, current, thrust, and specific impulse are shown. The simulations are designated as either chemical equilibrium (CE) or chemical nonequilibrium (CNE). For each case, the upstream anode surface 2A (Fig. 1) temperature is constant at $T_a = 1000$ K, and the cathode 1C temperature varies linearly from $T_c = 1000$ K at the inlet to $T_c = 3000$ K at the cathode tip. The constrictor diameter is 0.63 mm. The cathode gap spacing, as measured axially from the converging portion of the anode surface, is $x_{cat} = 0.58$ mm for the hydrazine cases and $x_{cat} = 1.8$ mm for the hydrogen case. An anode voltage drop of $V_s = 13.0$ V is assumed, and the anode emissivity is $\epsilon = 0.31$.[12] The inlet flow swirl velocity is 30% of the axial inflow velocity. The computational grids, shown in Fig. 3, are comprised of 62 axial by 17 radial nodes for the plasma, and 62 axial by 9 radial nodes for the anode domain. Simulation run time is several hours on a Convex C-240 mainframe computer.

1. Hydrazine Simulations

The CE and CNE hydrazine simulations are systematically compared in Figs. 4 - 15. Contours of current density and anode temperature are indicated in Fig. 4 for CE hydrazine. At the cathode tip, the current density is $j \approx 40,000$ A/cm^2. A peak anode attachment current density of $j \approx 18$ A/cm^2 is noted at a location of $x \approx 11$ mm, or roughly 5 mm downstream of the constrictor. The anode temperature increases from the upstream boundary value of $T_a = 1000$ K to $T_a \approx 1300$ K near the exit plane. The CNE hydrazine results are shown in Fig. 5. The peak anode current density of $j \approx 15$ A/cm^2 occurs at $x \approx 8$ mm, upstream from that for the CE case. The anode temperature is somewhat lower than for CE, with a value of $T_a \approx 1200$ K at the exit plane.

The marked difference in the current attachment predictions is more clearly illustrated in Fig. 6, where the anode current densities are indicated. For CNE, a more diffuse, bimodal distribution is noted, with the attachment closer to the constrictor. Consequently the voltage prediction, indicated in Table 4, is significantly lower at 87 V

for CNE versus 113 V for the CE simulation. The anode T_e distributions are indicated in Fig. 7. A high degree of thermal nonequilibrium is noted, with maximum electron temperatures of $T_e \approx 8{,}000$ K and $T_e \approx 12{,}000$ K for the CE and CNE simulations respectively.

Heavy species and electron temperature contours in the constrictor region are indicated in Figs. 8-11. In Fig. 8, a maximum $T_g \approx 22{,}000$ K occurs near the center of the constrictor for CE hydrazine. The central region of the arc is near thermal equilibrium, as indicated by a maximum $T_e \approx 23{,}500$ K shown in Fig. 9. The results for CNE hydrazine are similar, with maxima of $T_g \approx 20{,}000$ K and $T_e \approx 23{,}000$ K indicated in Figures 10 and 11.

Axial velocity contours are shown in Figs. 12 and 13. A maximum centerline velocity of $u \approx 8$ km/s occurs at $x = 8$ mm, and then decreases because of heating and viscous losses to $u \approx 6$ km/s at the exit for CE hydrazine. For CNE hydrazine, a maximum velocity of $u \approx 7$ km/s is predicted to occur at $x = 9$ mm, decreasing to $u \approx 6.5$ km/s at the exit.

Finite-rate chemistry must be included to capture frozen flow effects. In Figs. 14 and 15, exit plane predictions of electron number density n_e are presented. The predicted centerline density for CE hydrazine is $n_e = 1.6 \times 10^{11}$ cm^{-3}, while for CNE, the density is 3 orders of magnitude higher at $n_e = 1.6 \times 10^{14}$ cm^{-3}. Also shown are T_e and T_g profiles. More thermal nonequilibrium is indicated for the CE case with $T_e/T_g \approx 2.0$ at the centerline, while the CNE case is near equilibrium at $T_e/T_g \approx 1.1$.

2. Hydrogen Simulation

The results for the CNE hydrogen simulation are indicated in Figs. 16 - 20. Anode temperature and current density contours are shown in Fig. 16. The peak anode current density of $j = 16$ A/cm^2 occurs at the attachment location of $x \approx 8$ mm. Due to the higher specific power deposition, the thermal loading of the anode is somewhat more severe than for the hydrazine cases, with a predicted temperature near the exit plane of $T_a \approx 1400$ K. Profiles of T_e and j at the anode surface are shown in Fig. 17. The results are qualitatively similar to the CNE hydrazine case, with high thermal nonequilibrium of $T_e \approx 12{,}000$ K predicted in the current attachment region.

Heavy species and electron temperature contours are shown in Figs. 18 and 19. In Fig. 18, a peak temperature of $T_g \approx 13{,}500$ K is noted. The electron temperature is similar in the central region of the flow with $T_e \approx 14{,}000$ K indicated in Fig. 19. At a location of $x = 8$ mm, T_e decreases in the radial direction reaching a minimum of $T_e \approx 3700$ K at $r = 0.5$ mm. The electron temperature then increases, eventually reaching a value of $T_e \approx 12{,}000$ K at the anode surface. The electron temperature profile is qualitatively similar to the nonequilibrium predictions of Miller and Martinez-Sanchez[17] and Keefer et al.[16]

Axial velocity contours are shown in Fig. 20. A maximum centerline value of $u \approx 15$ km/s occurs at $x = 7$ mm decreasing to $u \approx 12$ km/s at the exit plane.

V. Conclusions

A detailed, propellant-flexible, N_2/H_2 arcjet model is developed, and is sufficiently comprehensive to be used for arcjet design studies. A thermal nonequilibrium, chemical equilibrium model was first developed, and then generalized to chemical nonequilibrium by including finite rate chemistry and mass diffusion. The incorporation of nonequilibrium processes permits the current distribution to be coupled to the plasma flowfield with realistic boundary conditions and without artificial modifications to the electrical conductivity.

Chemical equilibrium and nonequilibrium results have been compared for hydrazine. High near-anode thermal nonequilibrium is indicated in both cases with $T_e/T_g \approx 8$ and $T_e/T_g \approx 12$ for CE and CNE predictions respectively. In the constrictor, the central region of the arc is near thermal equilibrium with $T_e \approx T_g \approx 20{,}000$ K. Mass diffusion and finite rate chemistry dramatically affect the arc structure. The incorporation of these chemical nonequilibrium processes reduces the arc length and lowers the predicted operating voltage. Additionally, higher frozen flow losses are

noted. Predicted electron densities at the arcjet exit plane are three orders of magnitude higher with nonequilibrium chemistry.

Chemical nonequilibrium results have been presented for hydrogen. The results are qualitatively similar to those for hydrazine. However, lower arc temperatures are noted, with centerline $T_e \approx T_g \approx 14,000$ K in the constrictor.

The combined effects of viscous losses and supersonic heating were noted in all cases. Centerline axial velocities reach a maximum a few millimeters downstream of the constrictor, and then decrease to exit plane values of $u \approx 6$ km/s and $u \approx 12$ km/s for hydrazine and hydrogen respectively.

An anode temperature model was included. For CE hydrazine, maximum anode temperatures of $T_a \approx 1300$ K are predicted near the exit plane. For CNE hydrazine and hydrogen, maxima of $T_a \approx 1200$ and $T_a \approx 1400$ are predicted.

The model has generated much useful data; however, unresolved issues remain. The voltage predictions largely depend on the arc attachment location. We have found that parametrically increasing electron-molecule inelastic energy transfer increases the arc length. A more general physical model of electron-molecule inelastic transfer is required to describe accurately the near-anode transport properties. Additionally, a detailed electrical sheath model is needed to predict near-electrode voltage drops.

We postulate that the electron energy distribution may be non-maxwellian due to the high level of inelastic electron-molecule energy loss. We are considering a more complete description of the coupling between the electron energy and molecular internal energy modes. This may be required to describe the arc attachment and near-anode electrical conductivity more accurately.

The model must be compared with detailed experimental measurements of plasma properties for validation of both local and global performance predictions. Predictions from this model are compared with our experiments in Refs. 49 and 50.

VI. Acknowledgments

VII. References

[1]Wilbur P. J., Jahn, R. G., and Curran, F. C., "Space Electric Propulsion Plasmas," *IEEE Transactions on Plasma Science*, Vol. 19, No. 6, pp. 1167-1179, December, 1991.

[2]Butler, G. W., Cassidy, R. J., and King, D. Q., "Directions for Arcjet Technology Development," AIAA Paper 94-2652, 1994.

[3]Jack, J. R., "Theoretical Performance of Propellants Suitable for Electrothermal Jet Engines." *ARS Journal*, Vol. 31, p. 1685, 1961.

[4]John, R. R., Benett, S., Coss, L. A., Chen, M. M., and Connors, J. F., "Energy Addition and Loss Mechanisms in the Thermal Arcjet Engine," AIAA Paper 63-022, 1963.

[5]Topham, D. R., "The Electric Arc in a Constant Pressure Axial Gas Flow," *J.Physics D.Applied Physics*, Vol. 14, 1971.

[6]Glocker, B., Schrade, H. O., and Auweter-Kurtz, M., "Performance Calculation of Arcjet Thrusters: The Three Channel Model," IEPC Paper 93-187, 1993.

[7]Martinez-Sanchez, M., and Sakamoto A., "Simplified Analysis of Arcjet Thrusters," AIAA Paper 93-1904, 1993.

[8]Martinez-Sanchez, M., "Arcjet Modeling: Status and Prospects," AIAA Paper 94-2653, 1994.

[9]Butler, G. W., Kashiwa, B. A., and King, D. Q., "Numerical Modeling of Arcjet Performance," AIAA Paper 90-1474, 1990.

[10]Butler, G. W., and King, D. Q., "Single and Two Fluid Simulations of Arcjet Performance," AIAA Paper 92-3104, 1992.

[11]Butler, G.W., Kull, A.E., and King, D.Q., "Numerical Simulations of Hydrogen Arcjet Performance," IEPC Paper 93-249, 1993.

[12]Butler, G.W., Kull, A.E., and King, D.Q., "Single Fluid Simulations of Low Power Hydrogen Arcjets," AIAA Paper 94-2870, 1994.

[13]Rhodes, R. and Keefer, D., "Numerical Modeling of an Arcjet Thruster," AIAA Paper 90-2614, 1990.

[14]Rhodes, R. and Keefer, D., "Modeling Arcjet Space Thrusters," AIAA Paper 91-1994, 1991.

[15]Rhodes, R. and Keefer, D., "Non-Equilibrium Modeling of Hydrogen Arcjet Thrusters," IEPC Paper 93-217, 1993.

[16]Keefer, D., Burtner, D., Moeller, T., and Rhodes, R., "Multiplexed Laser Induced Flourescence and Non-Equilibrium Processes in Arcjets," AIAA Paper 94-2656, 1994.

[17]Miller, S. and Martinez-Sanchez, M., "Nonequilibrium Numerical Simulation of Radiation-Cooled Arcjet Thrusters," IEPC Paper 93-218, 1993. accepted for publication, *AIAA Journal of Propulsion and Power*, 1995, as "Two Fluid Nonequilibrium Simulation of Hydrogen Arcjet Thrusters."

[18]Flowe, A.C., DeWitt, K.J., Keith, T.G., Jr., Pawlas, G.E., Penko, P.F., "Numerical Modeling of Fluid and Electromagnetic Phenomena in an Arcjet," AIAA Paper 92-3106, 1992.

[19]Ciucci, A., d'Agostino, L., and Andrenucci, M., "Development of a Numerical Model of the Nozzle Flow in Low Power Arcjet Thrusters," IEPC Paper 93-182, 1993.

[20]Fujita, K. and Arakawa, Y., "Anode Heat Loss and Current Distributions of DC Arcjets," IEPC Paper 93-185, 1993.

[21]Babu, V., Aithal, S., and Subramaniam V. V., "On the Effects of Swirl in Arcjet Thruster Flows," IEPC Paper 93-183, 1993.

[22]Babu, V., Aithal, S., and Subramaniam V. V., IEPC Paper 93-129, 1993.

[23]Kruger, C.H., and Mitchner, M., "Kinetic Theory of Two Temperature Plasmas," *Physics of Fluids*, Vol. 10, No. 9, pp. 1953-1961, September 1967.

[24]Mertogul, A. E., "Modeling and Experimental Measurements of Laser Sustained Plasmas," Ph.D. Thesis, Department of Mechanical and Industrial Engineering, University of Illinois at Urbana-Champaign, 1993.

[25]Sutton and Sherman, Engineering Magneto-Hydrodynamics, McGraw-Hill, New York, 1965.

[26]McCay, D. T., and Dexter C. E., "Chemical Kinetic Performance Losses for a Hydrogen Laser Thermal Thruster," *J. Spacecraft*, Vol. 24, No. 4, pp.372-6.

[27]Janev, et. al, Elementary Processes in Hydrogen Helium Plasmas, Springer-Verlag, New York, 1987.

[28]Cambier, J-L., and Moreau, S., "Simulations of a Molecular Plasma in Collisional-Radiative Nonequilibrium," AIAA Paper 93-3196, 1993.

[29]Park, C., Nonequilibrium Hypersonic Aerothermodynamics, John Wiley and Sons, New York, 1990.

[30]Incropera, F. P., and Dewitt, D. P., Fundamentals of Heat and Mass Transfer, John Wiley & Sons, New York, 1981, p. 758.

[31]van de Sanden, M. C. M., Schram, P. P. J. M., Peeters, A. G., van der Mullen, J. A. M., and Kroesen, G. M. W., "Thermodynamic Generalization of the Saha Equation for a Two-Temperature Plasma," *Physical Review A*, Vol. 40, No. 9, pp 5273-5276, The American Physical Society, 1989.

[32]Eddy, T. L., Leger, J. M., Coudert, Fauchais P., "Nonequilibrium Diagnostics of a Nitrogen Plasma Jet," HTD-Vol. 161, *Heat Transfer in Thermal Processing*, ASME, 1991.

[33]Fan, W. X. and Dudeck, M. A., "A Study of Concentraions in A Nitrogen Plasma Under Thermal Unbalance Conditions," *J. Chem. Phys.*, Vol. 88, pp 27-37, Elsivier, Paris, 1991.

[34]Drellishak, K. S., Partition Functions and Thermodynamic Properties of High Temperature Gases, Ph.D. Thesis, Northwestern University, 1963.

[35]Mitchner, M., and Kruger, C., Partially Ionized Gases, John Wiley and Sons, New York, 1973.

[36]Maitland, G. C., Rigby, M., Smith, B. E., Wakeham, W. A., Intermolecular Forces, Clarendon Press, Oxford, 1981, p 302.

[37]Capecchi, G. and d'Agostino, L., "Numerical Model of Equilibrium Composition and Transport Coefficients of Hydrazine under Dissociation and Ionization," AIAA Paper 94-2868, 1994.

[38]Stallcop, J. R., Partridge, H., and Levin, E., "Resonance Charge Transfer, Transport Cross Sections, and Collision Integrals for $N^+(^3P)$-$N(^4S^0)$ and $O^+(^4S^0)$-$O(^3P)$ Interactions," *J. Chem. Phys*, Vol. 95, No. 9, pp. 6429-6439, American Institute of Physics, Nov., 1991.

[39]Stallcop, J. R., Bauschlicher, C. W., Partridge, H., and Levin, E., "Theoretical Study of Hydrogen and Nitrogen Interactions: N-H Transport Cross Sections and Collision Integrals,"*J. Chem. Phys*, Vol. 97, No. 8, pp. 5578-5585, American Institute of Physics, Oct., 1992.

[40]Levin, E., Partridge, H., and Stallcop, J. R., "Collision Integrals and High Temperature transport Properties for N-N, O-O, and N-O," *J. Thermophysics*, Vol. 4, No. 4, pp. 469-477, Mitchner Oct. 1990.

[41]Vanderslice, J. T., *et. al*, "High Temperature Transport Properties of Dissociating Hydrogen," *The Physics of Fluids*, Vol. 5, No. 2, pp. 155-164, Feb., 1962.

[42]Stallcop, J. R., Partridge, H., Walch, S. P., and Levin, E., "H-N$_2$ Interaction Energies, Transport Cross Sections, and Collision Integrals," *J. Chem. Phys.*, Vol. 97, No. 5, pp. 3431-3436, American Institute of Physics, Sept., 1992.

[43]Grier, N. T., "Calculation of Transport Properties of Ionizing Atomic Hydrogen," NASA TN D-1386, National Aeronautics and Space Administration, Washington, D. C., Apr., 1966.

[44]Chang, C. H. and Pfender, E., "Nonequilibrium Modeling of Low Pressure Argon Plasma Jets; Part I: Laminar Flow," *Plasma Chemistry and Plasma Processing*, Vol. 10, No. 3, pp. 473-491, 1990.

[45]Burton, R. L., Bufton, S. A., Tiliakos, N. T., and Krier, H., "Application of Multiple Electrostatic Probes to a Low Power Arcjet," AIAA Paper 94-3299, 1994.

[46]Issa, R. I., "Solution of the Implicitly Discretised Fluid Flow Equations by Operator-Splitting," *Journal of Computational Physics*, Vol. 62, pp. 40-65, 1986.

[47]Rhie, C. M., "A Pressure-Based Navier Stokes Solver Using The Multigrid Method," AIAA Paper 86-0207, 1986.

[48]Karki, K.C., A Calculation Procedure for Viscous Flows at All Speeds in Complex Geometries, Ph.D. Thesis, University of Minnesota, 1986.

[49]Bufton, S. A., Burton, R. L., and Krier, H., "Measured Plasma Properties at the Exit Plane of a 1 kW Arcjet," AIAA Paper 95-3066, 31st Joint Propulsion Conference, San Diego, July, 1995.

[50]Tiliakos, N. T>, Burton, R. L., and Krier, H., "Application of Internal Langmuir Diagnostics for Arcjets," AIAA Paper 95-2386, 31st Joint Propulsion Conference, San Diego, July, 1995.

VIII. Figures and Tables

species	C_{pi} (J/K)	h_i^0 (J/particle)
e	$5/2\, k_b$	0
H$_2$	$k_b\left(7/2 + \dfrac{\theta_{vH2}}{T_g}\left(e^{\theta_{vH2}/T_g} - 1\right)^{-1}\right)$	$k_b/2\, \theta_{vH2}$
N$_2$	$k_b\left(7/2 + \dfrac{\theta_{vN2}}{T_g}\left(e^{\theta_{vN2}/T_g} - 1\right)^{-1}\right)$	$k_b/2\, \theta_{vN2}$
H	$5/2\, k_b$	$1/2\, \varepsilon_{d,H2}$
N	$5/2\, k_b$	$1/2\, \varepsilon_{d,N2}$
H$^+$	$5/2\, k_b$	$1/2\, \varepsilon_{d,H2} + \varepsilon_{i,H}$
N$^+$	$5/2\, k_b$	$1/2\, \varepsilon_{d,N2} + \varepsilon_{i,N}$

Table 1: Species reference enthalpies and specific heats.

Reaction*	Rate (m^6/s or m^3/s)	Loss rate (W/m^3)	Ref.
2H + M = H$_2$ + M	$k_{fl} = \dfrac{1.764 \times 10^{-42}}{T_g}$	$L_h = \left(k_{rl}n_{H2} - k_{fl}n_H^2\right) n_M \varepsilon_{d,H2}$	26

$H^+ + e + M = H + M$	$k_{f2} = \dfrac{1.45 \times 10^{-33}}{T_g^{2.5}}$	$L_h = (k_{r2}n_H - k_{f2}n_{H^+}n_e)\, n_M \varepsilon_{i,H}$	26
$e + H_2 \longrightarrow 2H + e$	$k_{f3} = \langle \sigma v \rangle$	$L_e = k_{f3}n_e n_{H2}\varepsilon_{d,H2}$	27
$H^+ + e \longrightarrow H + h\nu$	$k_{f4} = \dfrac{6.26 \times 10^{-17}}{T_e^{0.58}}$	$L_e = k_{f4}n_e n_{H^+}\varepsilon_{i,H}$	26
$H^+ + 2e = H + e$	$k_{f5} = \dfrac{1.95 \times 10^{-20}}{T_e^{4.5}}$	$L_e = (k_{r6}n_H - k_{f6}n_e n_{H^+})n_e \varepsilon_{i,H}$	26
$N_2 + M \longrightarrow 2N + M$	$k_{f7} = \dfrac{6.14 \times 10^{-9}}{T_g^{1.6}} e^{-113,200/T_g}$	$L_h = k_{f7}n_{N2}n_M \varepsilon_{d,N2}$	28
$M + 2N \longrightarrow N_2 + M$	$k_{f8} = \dfrac{8.10 \times 10^{-37}}{T_g^{1.39}} e^{1745/T_g}$	$L_h = - k_{f8}n_N^2 n_M \varepsilon_{d,N2}$	28
$e + N_2 \longrightarrow 2N + e$	$k_{f9} = \dfrac{4.98 \times 10^{-6}}{T_e^{1.6}} e^{-113,200/T_e}$	$L_e = k_{f9}n_e n_{N2}\varepsilon_{d,N2}$	29
$N + e = N^+ + 2e$	$k_{f10} = \dfrac{4.15 \times 10^{3}}{T_e^{3.82}} e^{-168,200/T_e}$	$L_e = (k_{f10}n_N - k_{r10}n_e n_{N^+})n_e \varepsilon_{i,N}$	29

Table 2: Finite rate chemistry model. * ---> one way reactions, = two way reactions with the reverse rate evaluated using the chemical equilibrium constants, M is any heavy species third body.
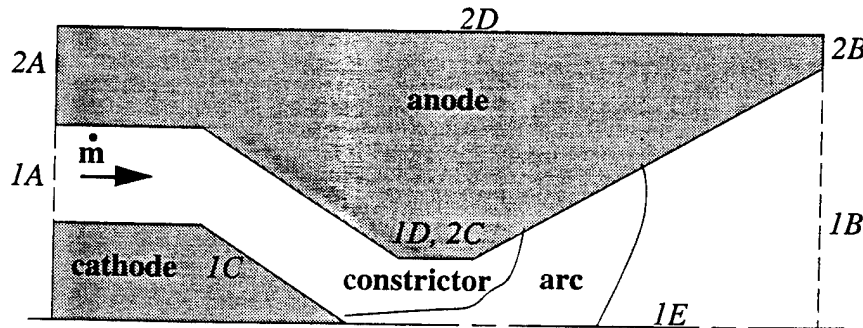
Figure 1: Schematic of arcjet thruster indicating fluid and anode domain boundaries.

Flow-Field Domain					
variable	*1A*	*1B*	*1C*	*1D*	*1E*
u	from stagnation properties	from momentum	$= 0$	$= 0$	$\frac{\partial u}{\partial r} = 0$
v	$= 0$	extrapolated	$= 0$	$= 0$	$= 0$
w	specified	extrapolated	$= 0$	$= 0$	$= 0$
T_e	$\frac{\partial T_e}{\partial x} = 0$	extrapolated	$\frac{\partial T_e}{\partial r} = 0$	$\frac{\partial T_e}{\partial r} = 0$	$\frac{\partial T_e}{\partial r} = 0$
T_g	from M and T_t	extrapolated	specified	$T_g = T_a$	$\frac{\partial T_g}{\partial r} = 0$
P	extrapolated	extrapolated	$\frac{\partial P}{\partial n} = 0$	$\frac{\partial P}{\partial n} = 0$	$\frac{\partial P}{\partial r} = 0$
V	$\frac{\partial V}{\partial x} = 0$	$\frac{\partial V}{\partial x} = 0$	$V = V_{cat}$	$V = V_s$	$\frac{\partial V}{\partial r} = 0$
Anode Domain					
variable	*2A*	*2B*	*2C*		*2D*
T_a	T_a specified or $\frac{\partial T_a}{\partial x} = 0$	$\dot{q} = \varepsilon\sigma\left(T_s^4 - T_{bg}^4\right)$	$\dot{q} = \lambda_h \frac{\partial T_g}{\partial n} + \lvert j \rvert V_s + \sum_{i=1}^{N} \frac{1}{m_i} \rho\left(C_{pi}T_i + h_i^0\right)D_i\frac{\partial y_i}{\partial n} - \varepsilon \sin 20°\sigma\left(T_s^4 - T_{bg}^4\right)$		$\dot{q} = \varepsilon\sigma\left(T_s^4 - T_{bg}^4\right)$

Table 3: Boundary conditions for the fluid dynamic, energy, and electromagnetic equations. Energy equation boundary conditions are shown for both the fluid and anode domains. For radiative boundary conditions, T_s is the local anode surface temperature.

CE/CNE	Propellant	$\dot{m}$ (mg/s)	I (Amps)	Voltage	I_{sp} (s)	Thrust (N)
CE	N_2H_4	52.9	10	113	441	0.229
CNE	N_2H_4	50.2	10	87	439	0.216
CNE	H_2	13.2	10	138	934	0.121

Table 4: Summary of predictions. CE denotes chemical equilibrium and CNE denotes chemical non-equilibrium simulations.
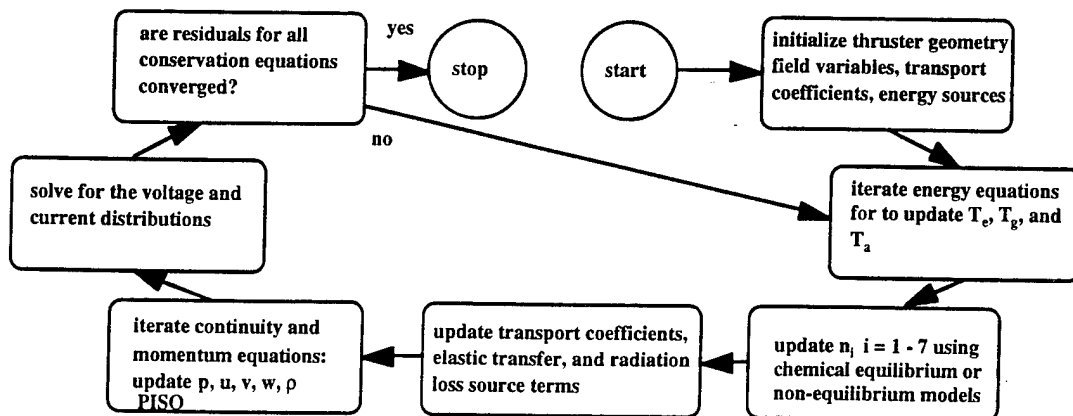
Figure 2: Numerical solution algorithm. The solution method is iterative, employing successive under-relaxation of the indicated field variables.
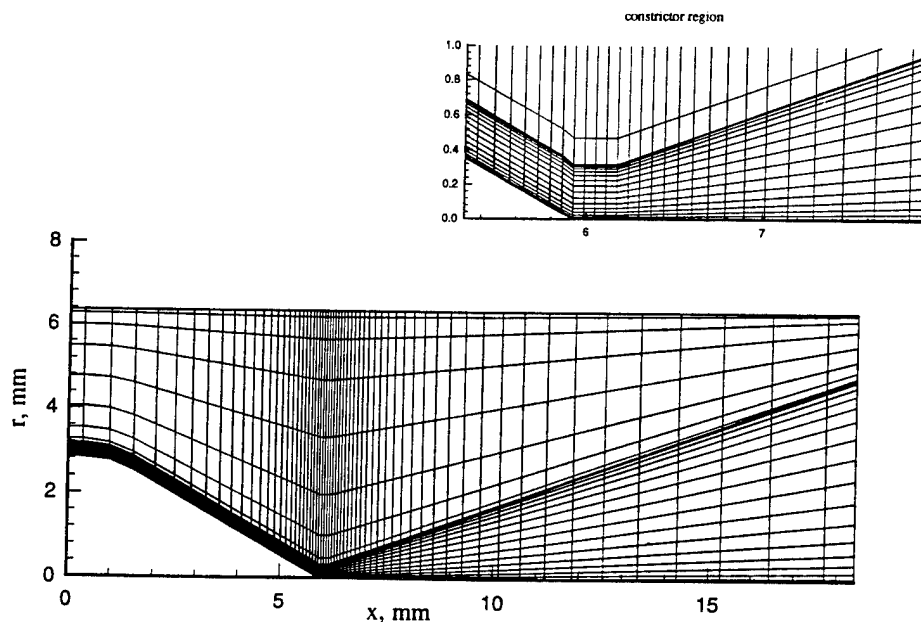

Figure 3: Computational grids. The grid is tuned axially for high density in the constrictor and radially for high density near the electrode surfaces.
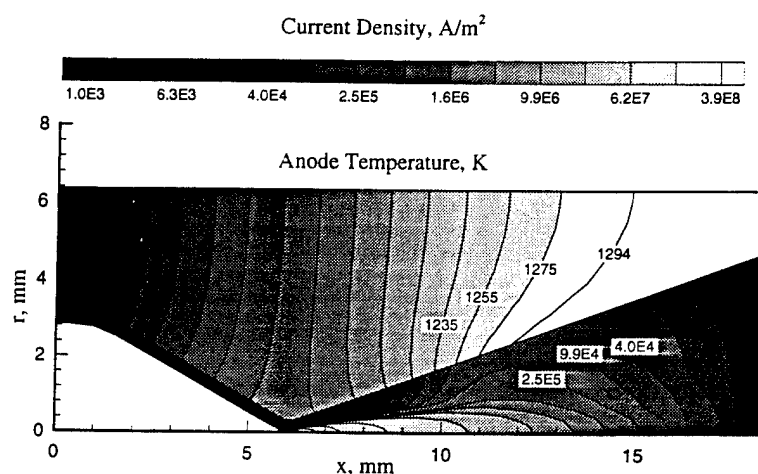
Figure 4: Anode temperature and current density for hydrazine; chemical equilibrium (CE) simulation. The maximum anode current density is $j \approx 18$ A/cm^2 at $x \approx 11$ mm.
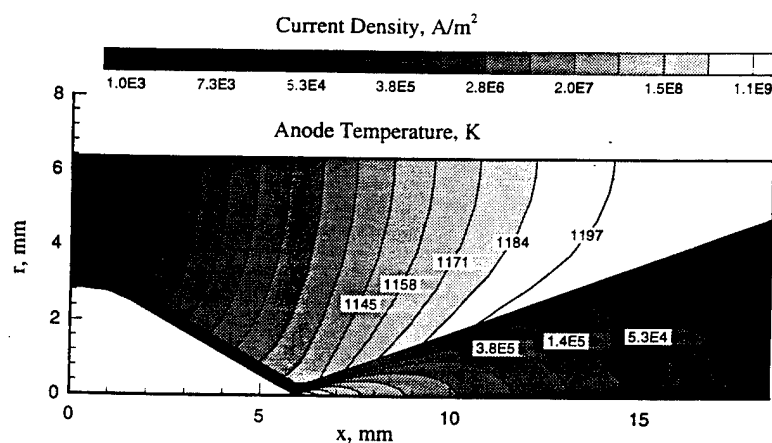
Figure 5: Anode temperature and current density for hydrazine; chemical nonequilibrium (CNE) simulation. The maximum anode current density is $j \approx 15$ A/cm^2 at $x \approx 8$ mm.
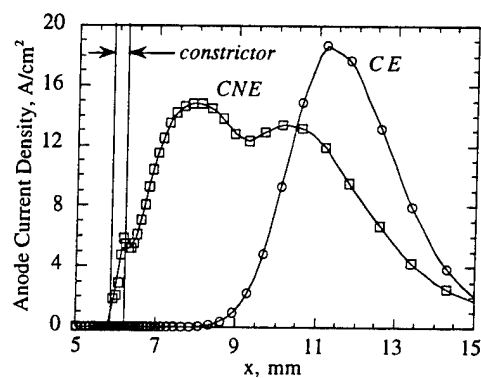
Figure 6: Current density at the anode surface for hydrazine. Results are shown for chemical equilibrium (CE) and chemical nonequilibrium (CNE) simulations.
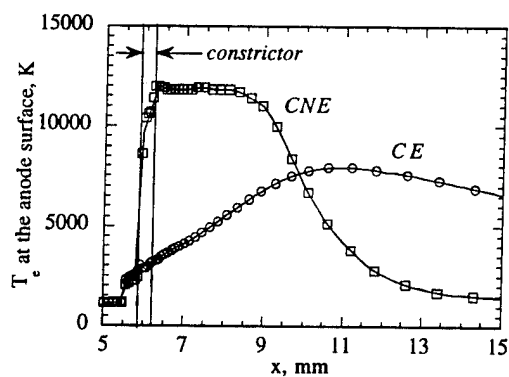
Figure 7: Electron temperature at the anode surface for hydrazine. Results are shown for chemical equilibrium (CE) and chemical nonequilibrium (CNE) simulations.
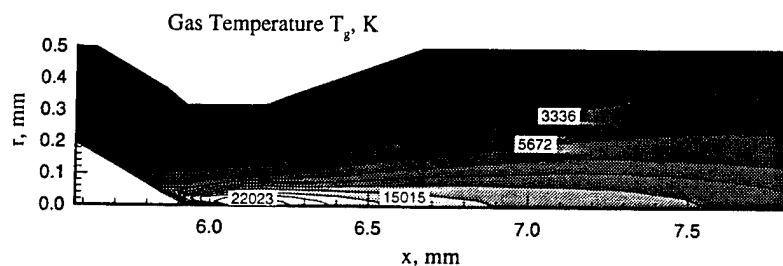
Figure 8: Heavy species temperature for hydrazine; chemical equilibrium (CE) simulation. The maximum is $T_g \approx 22,000$ K at the constrictor centerline. The exit plane is located at x = 18.5 mm.
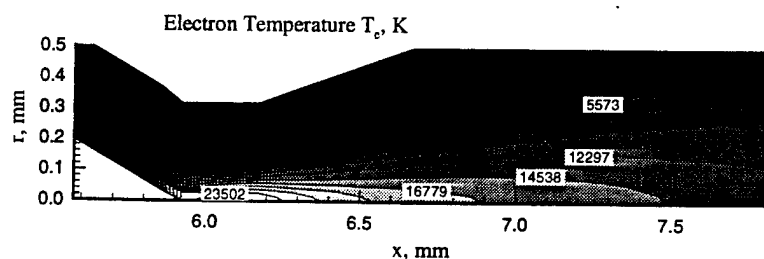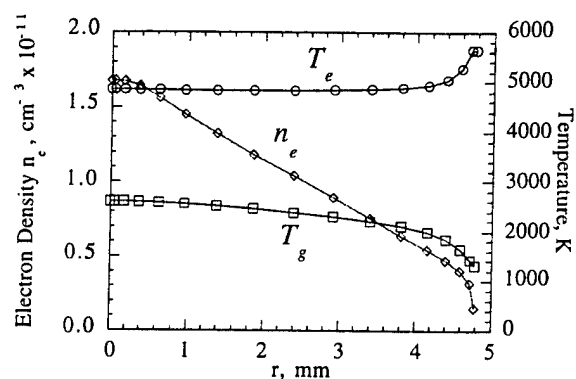

Figure 9: Electron temperature for hydrazine; chemical equilibrium (CE) simulation. The maximum is $T_e \approx 23,500$ K at the constrictor centerline. The exit plane is located at x = 18.5 mm.
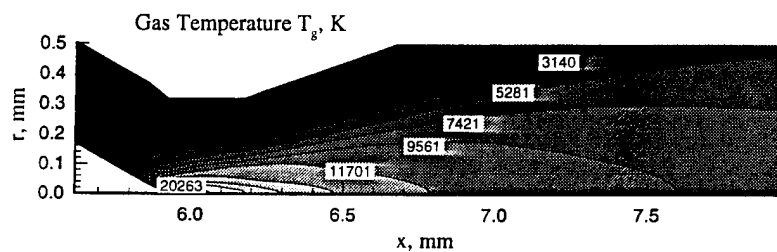
Figure 10: Heavy species temperature for hydrazine; chemical nonequilibrium (CNE) simulation. The maximum is $T_g \approx 20{,}000$ K at the constrictor centerline. The exit plane is located at x = 18.5 mm.
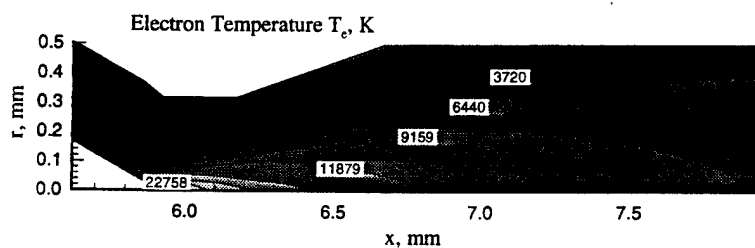
Figure 11: Electron temperature for hydrazine; chemical nonequilibrium (CNE) simulation. The maximum is $T_e \approx 23{,}000$ K at the constrictor centerline. The exit plane is located at x = 18.5 mm.
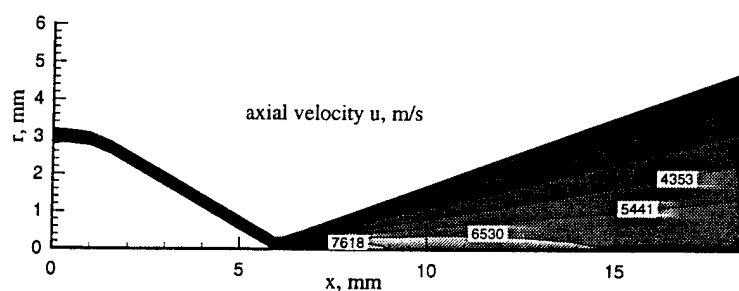
Figure 12: Axial velocity contours for hydrazine; chemical equilibrium (CE) simulation. The maximum is u ≈ 8 km/s at x ≈ 8 mm. The centerline velocity decreases to u ≈ 6 km/s at the exit plane.
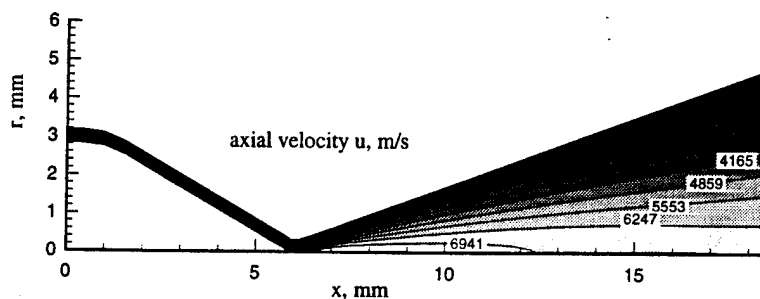

Figure 13: Axial velocity contours for hydrazine; chemical nonequilibrium (CNE) simulation. The maximum is u ≈ 7 km/s at x ≈ 9 mm. The centerline velocity decreases to u ≈ 6.3 km/s at the exit plane.

Figure 14: Radial distributions of electron density, electron temperature, and heavy species temperature at the exit plane for hydrazine; chemical equilibrium (CE) simulation.
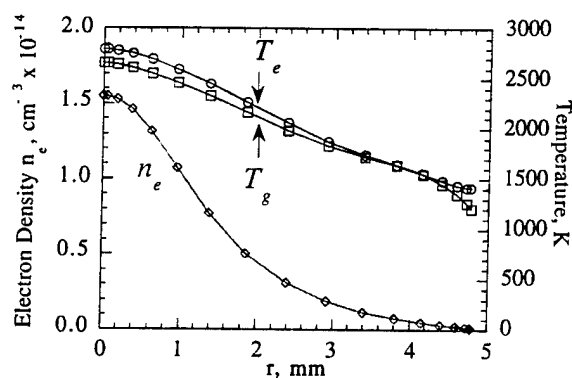

Figure 15: Radial distributions of electron density, electron temperature, and heavy species temperature at the exit plane for hydrazine; chemical nonequilibrium (CNE) simulation.
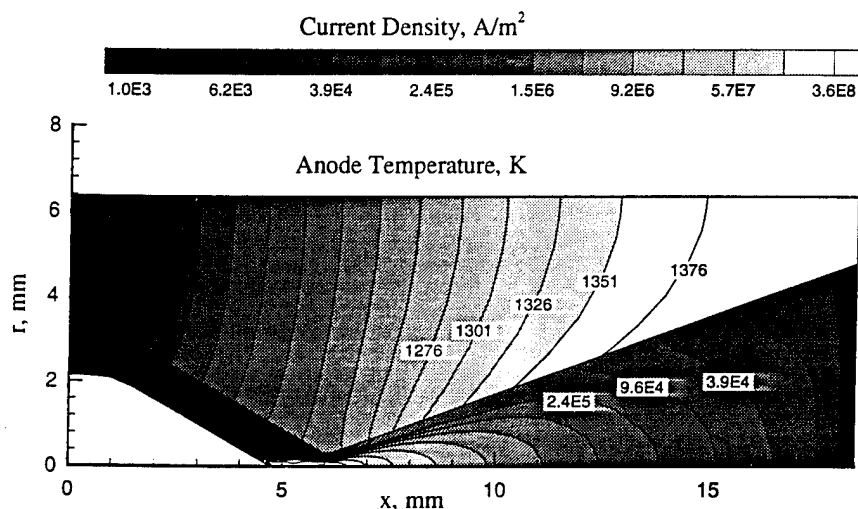
Figure 16: Anode temperature and current density for hydrogen; chemical nonequilibrium (CNE) simulation. The maximum anode current density is j ≈ 16 A/cm^2 at x ≈ 8 mm.
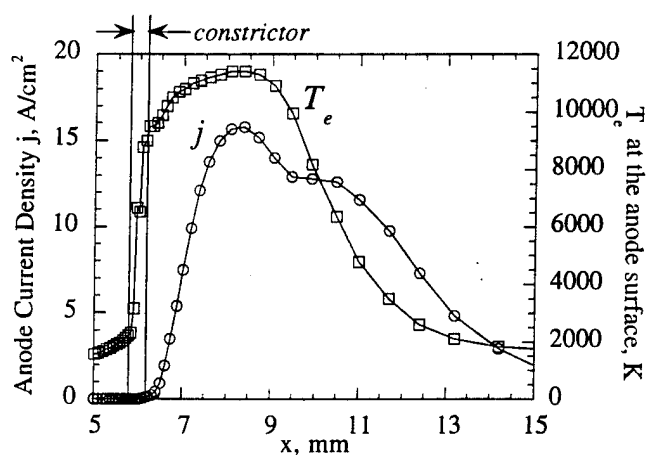

Figure 17: Electron temperature and current density at the anode surface for hydrogen; chemical nonequilibrium (CNE) simulation.
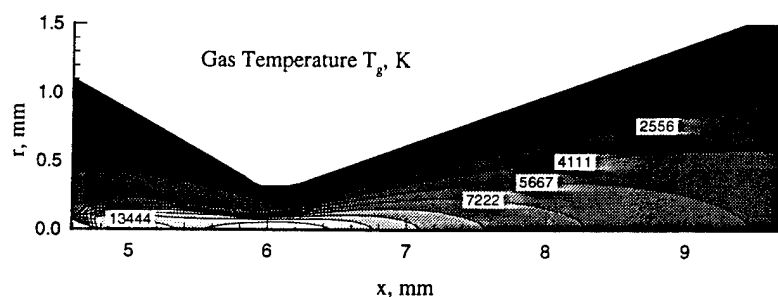
Figure 18: Heavy species temperature for hydrogen; chemical nonequilibrium (CNE) simulation. The maximum is $T_g \approx 13{,}500$ K at the centerline near the cathode tip. The exit plane is located at x = 18.5 mm.
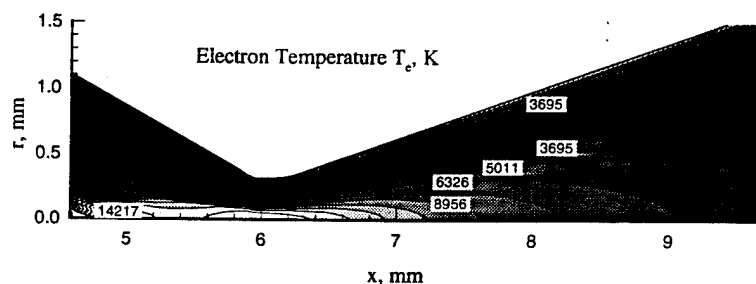
Figure 19: Electron temperature for hydrogen; chemical nonequilibrium (CNE) simulation. The maximum is $T_e \approx 14{,}000$ K at the centerline near the cathode tip. High near-anode thermal nonequilibrium is indicated downstream of the constrictor, with $T_e \approx 12{,}000$ K at the anode surface. The exit plane is located at x = 18.5 mm.
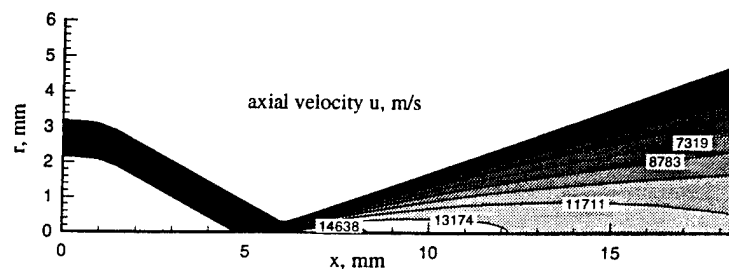
Figure 20: Axial velocity contours for hydrogen; chemical nonequilibrium (CNE) simulation. The maximum is u ≈ 15 km/s at x ≈ 8 mm. The centerline velocity decreases to u ≈ 12 km/s at the exit plane.